Mathematical Models of Retinitis Pigmentosa: The Oxygen Toxicity Hypothesis

Paul A. Roberts[a,b,1,*], Eamonn A. Gaffney[c], Philip J. Luthert[d], Alexander J. E. Foss[e], Helen M. Byrne[c]

[a]*Mathematical Institute, University of Oxford, Andrew Wiles Building, Radcliffe Observatory Quarter, Woodstock Road, Oxford, OX2 6GG, UK*
[b]*Department of Computer Science, University of Oxford, Wolfson Building, Parks Road, Oxford, OX1 3QD, UK*
[c]*Wolfson Centre for Mathematical Biology, Mathematical Institute, University of Oxford, Andrew Wiles Building, Radcliffe Observatory Quarter, Woodstock Road, Oxford, OX2 6GG, UK*
[d]*Institute of Ophthalmology, University College London, 11-43 Bath Street, London, EC1V 9EL, UK*
[e]*Queen's Medical Centre, Department of Ophthalmology, Derby Road, Nottingham, Nottinghamshire, NG7 2UH, UK*

Abstract

The group of genetically mediated diseases, known collectively as retinitis pigmentosa (RP), cause retinal degeneration and, hence, loss of vision. The most common inherited retinal degeneration, RP is currently untreatable. The retina detects light using cells known as photoreceptors, of which there are two types: rods and cones. In RP, genetic mutations cause patches of photoreceptors to degenerate and typically directly affect either rods or cones, but not both. During disease progression, degenerate patches spread and the unaffected photoreceptor type also begins to degenerate. The cause underlying these phenomena is currently unknown.

The oxygen toxicity hypothesis proposes that secondary photoreceptor loss is due to hyperoxia (toxically high oxygen levels), which results from the decrease in oxygen uptake following the initial loss of photoreceptors. In this paper, we construct mathematical models, formulated as 1D systems of partial differential equations, to investigate this hypothesis. Using a combination of numerical simulations, asymptotic analysis and travelling wave analysis, we find that degeneration may spread due to hyperoxia, and generate spatio-temporal patterns of degeneration similar to those seen *in vivo*. We determine the conditions under which a degenerate patch will spread and show that the wave speed of degeneration is a monotone decreasing function of the local photoreceptor density. Lastly, the effects of treatment with antioxidants and trophic factors, and of capillary loss, upon the dynamics of photoreceptor loss and recovery are considered.

Keywords: Partial Differential Equations, Asymptotic Analysis, Retina, Photoreceptors, Hyperoxia

1. Introduction

The term retinitis pigmentosa (RP) refers to a group of genetically mediated retinal degenerative diseases that cause a progressive loss of visual function. RP is the most common inherited retinal degeneration, with

[*]Corresponding author
Email addresses: p.a.roberts@univ.oxon.org (Paul A. Roberts), gaffney@maths.ox.ac.uk (Eamonn A. Gaffney), p.luthert@ucl.ac.uk (Philip J. Luthert), alexander.foss@nottingham.ac.uk (Alexander J. E. Foss), helen.byrne@maths.ox.ac.uk (Helen M. Byrne)
[1]Present address: School of Mathematics, University of Birmingham, Edgbaston Campus, Birmingham, B15 2TT, UK

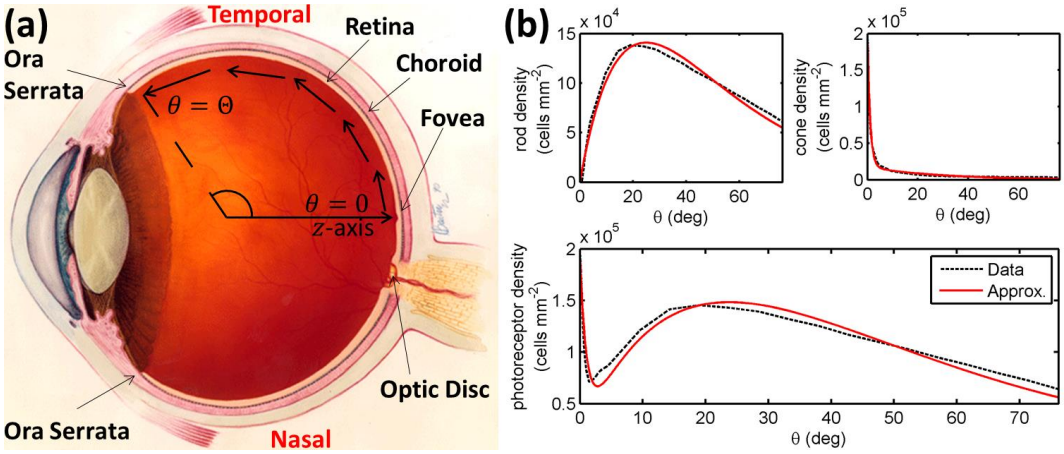

Figure 1: Diagrams of the human eye and retinal photoreceptor distribution. (a) Diagram of the (right) human eye, viewed in the transverse plane. The diagram shows the model geometry: the domain is located between the foveal centre, at $\theta = 0$, and the ora serrata, at $\theta = \Theta$, along the temporal horizontal meridian, where θ measures the eccentricity. Figure reproduced, with modifications, from `http://www.nei.nih.gov/health/coloboma/coloboma.asp`, courtesy: National Eye Institute, National Institutes of Health (NEI/NIH). (b) Graphs to show measured and fitted photoreceptor profiles, along the temporal horizontal meridian, in the human retina. Cone profile: $B_1 e^{-b_1\theta} + B_2 e^{-b_2\theta}$, and rod profile: $B_3\theta e^{-b_3\theta}$ (see the Supplementary Materials for parameter values). The photoreceptor profile is the sum of the rod and cone profiles. Experimental data provided by Curcio and published in Curcio et al. (1990).

a prevalence (in its nonsyndromic form) of 1 in 4000, corresponding to a total of 1.5 million affected individuals worldwide (Hamel, 2006; Hartong et al., 2006; Shintani et al., 2009). At present no treatments are clinically available either to slow its progression or reverse its effects (Musarella and MacDonald, 2011). In this paper, we investigate the prospective role of oxygen toxicity (or hyperoxia) in the progression of RP.

The retina is the innermost (closest to the centre of the eye) tissue layer in the eye, extending from the optic disc, where the optic nerve, central retinal artery and vein puncture the retina, to the ora serrata (Figure 1(a)). The outer (furthest from the centre of the eye) layer of the retina, with which we are concerned here, is mainly populated by two types of cell: photoreceptors and retinal pigment epithelium (RPE) cells. The light-detecting photoreceptors come in two varieties: rods, which confer achromatic vision under scotopic (low light) conditions and cones, which provide high-acuity colour vision under photopic (well-lit) conditions.

The outer parts of the photoreceptors are composed of inner segments (ISs) and outer segments (OSs). The ISs contain most of a photoreceptor's mitochondria, constituting their primary site of oxygen consumption, whilst the OSs are composed of discs in which light-sensitive photopigments are embedded. Discs are periodically shed from the tips of OSs, where they are phagocytosed by the overlying RPE cells, and are regenerated at the OS base, with a turnover rate of 9–13 days (Young, 1971, see also Oyster, 1999; Young, 1967, 1978; Young and Bok, 1969).

The average human retina contains 92 million rods and 4.6 million cones (Curcio et al., 1990). Figure 1(b) shows the distribution of rods and cones in a typical human retina. Cones attain their highest density in a sharp peak centred at zero degrees eccentricity, in a region known as the fovea (see Figure 1(a)), their density falling off rapidly with increasing eccentricity, whilst rods are absent from the centre of the fovea, their density increasing sharply with increasing eccentricity, reaching a maximum at around 20 degrees, before falling off more gradually toward the periphery. Thus the fovea is cone dominated, whilst the rest of the retina is rod dominated. Both rods and cones are absent from the optic disc.

Oxygen is delivered to the retina via two blood supplies: the choriocapillaris (CC), a capillary bed forming the innermost layer of a vascular layer known as the choroid, supplies the outer retina, whilst the retinal capillaries mainly supply the inner retina (Wangsa-Wirawan and Linsenmeier, 2003; Yu and Cringle, 2001).

RP usually exhibits as a rod-cone dystrophy, meaning that rods are affected earlier and more severely than cones (Hamel, 2006). However, less common forms exist, in which rod and cone loss occurs on the same timescale, or in which cone loss precedes rod loss (termed a cone-rod dystrophy; Hartong et al., 2006). Histological data from humans and rats suggest that the initial loss of photoreceptors occurs in roughly circular patches which expand and coalesce over time (Cideciyan et al., 1998; García-Ayuso et al., 2013; Ji et al., 2012; Lee et al., 2011; Zhu et al., 2013). Whilst the initial loss of photoreceptors is due directly to a mutation, it is not known what causes degenerate patches to spread, or what causes cone loss to follow rod loss in the rod-cone dystrophy form (and vice-versa in the cone-rod dystrophy form).

Four main hypotheses have been proposed to explain these phenomena. Firstly, the rod trophic factor hypothesis suggests that rods produce a trophic factor necessary for cone survival, such that, when rods are lost, this factor is depleted, leading to cone loss (Fintz et al., 2003; Léveillard et al., 2004; Mohand-Saïd et al., 1997, 1998, 2000). Secondly, the toxic substance hypothesis suggests that dying photoreceptors may release toxic substances into their surroundings, poisoning nearby photoreceptors (Ripps, 2002). Thirdly, the microglia hypothesis suggests that microglia cells are activated by rod death to release toxic factors, resulting in the death of the surrounding photoreceptors (Gupta et al., 2003).

In this paper we develop mathematical models to test the fourth hypothesis, known as the oxygen toxicity hypothesis; first suggested by Travis et al. (1991) and later developed by Valter et al. (1998) and Stone et al. (1999). Following an initial loss of photoreceptors, the oxygen demand in the outer retina is significantly decreased, resulting in an increase in outer retinal oxygen concentrations (Padnick-Silver et al., 2006; Stone et al., 1999; Yu et al., 2000, 2004). These oxygen levels are maintained due to the inability of the choroid to autoregulate in response to increased outer retinal oxygen concentrations (Stone et al., 1999; Yu et al., 2004; Yu and Cringle, 2005). This creates a toxic environment for the remaining rod and cone ISs (Stone et al., 1999; Travis et al., 1991), resulting in a positive feedback loop, as high oxygen levels cause photoreceptor death, which in turn increases oxygen levels. High oxygen levels are toxic to photoreceptors, since they result in an excess of reactive oxygen species, which cause damage to lipids, proteins and DNA (Shen et al., 2005). Studies using human epithelial cells (Wang et al., 2003) and rd1 mouse photoreceptors (Sahaboglu et al., 2013) show that cells take about 72 hours to die from hyperoxia. This corresponds to a timescale of decades for degeneration to spread across the retina (given that approximately 4000 photoreceptors lie along any direct path traced through the retina between the ora serrata and the fovea and assuming sequential cell death), a timescale consistent with degeneration in humans (Hartong et al., 2006). Further evidence supporting the role of hyperoxia in RP can be found in Cingolani et al. (2006); Wellard et al. (2005); Yamada et al. (1999); for reviews, see Roberts (2015); Stone et al. (1999); Yu and Cringle (2001, 2005).

Treatment with antioxidants and trophic factors has been shown to improve photoreceptor survival in RP: antioxidants neutralise the excess of reactive oxygen species produced under hyperoxia (Kohen and Nyska, 2002), whilst trophic factors increase photoreceptor resistance to apoptosis (Dong et al., 2006; Kohen and Nyska, 2002; Komeima et al., 2006, 2007; Okoye et al., 2003; Sanz et al., 2007; Yamada et al., 2001; Yu et al., 2004).

Degeneration of the CC is commonly observed in human models of RP, although its immediate cause is unknown (Li et al., 1995; Milam et al., 1998; Mullins et al., 2012). The CC is usually absent from areas in which photoreceptors have completely degenerated and in which RPE cells have migrated away from the CC, towards the retinal capillary layers (Li et al., 1995; Milam et al., 1998), suggesting that the loss of photoreceptors and RPE is either directly or indirectly responsible for CC degeneration (see Roberts, 2015,

for a detailed discussion). It has been shown that the CC degenerates within one week after the removal of the RPE (Del Priore et al., 1996); however, to the best of our knowledge, the rate of CC degeneration in RP has not been measured. Since capillary degeneration in the CC leads to a decrease in oxygen supply, this modulates the hyperoxia-driven progression of photoreceptor degeneration. We note that, from this point onwards, we use the term 'capillaries' to refer to the capillaries in the CC (rather than the retinal capillaries).

Whilst the precise mechanisms underlying RP have yet to be determined, the spatio-temporal patterns of retinal degeneration are well-defined. In particular, Grover et al. (1998) have identified three distinct patterns of visual field loss in human RP. Pattern 1 involves the concentric loss of vision, starting at the far-periphery, sometimes accompanied by a parafoveal or perifoveal ring scotoma (blind spot), whilst patterns 2 and 3 involve preferential loss of mid-peripheral vision. In all cases the central visual field is preserved, being lost only at the end stage of the disease. Studies by Escher et al. (2012); Lima et al. (2009, 2012); Murakami et al. (2008); Popović et al. (2005); Robson et al. (2003, 2004, 2006, 2008, 2011) describe similar patterns of degeneration.

To date, few mathematical models have been developed to study retinal degeneration in general and RP in particular (see Roberts et al., 2016, for a detailed review). Colón Vélez et al. (2003); Camacho et al. (2010); Camacho and Wirkus (2013); Camacho et al. (2014, 2016a,b) and Camacho et al. (2016c) have produced a series of spatially-averaged ordinary differential equation (ODE) models examining the rod trophic factor hypothesis. Their work suggests the importance of rod trophic factor to the survival of both rods and cones. They were also able to trace the progression of the disease through distinct physiological stages and to suggest optimal treatment strategies for RP under this hypothesis. Building on the experimental work of Clarke et al. (2000, 2001), Burns et al. (2002) constructed a spatially explicit 1D partial differential equation (PDE) model, to examine the toxic substance hypothesis. The model captures the initial patchy loss of photoreceptors as well as the exponential decline in photoreceptor number measured by Clarke et al. (2000, 2001) (see also, Clarke and Lumsden, 2005a,b; Lomasko et al., 2007a,b; Lomasko and Lumsden, 2009).

In this paper, we use mathematical models to explore, for the first time, the oxygen toxicity hypothesis. Our models combine some of the strengths of previous modelling work, in that they are spatially explicit, and distinguish between rods and cones. In addition, they are the first to account for the heterogeneous distribution of rods and cones, and its effects upon the spatio-temporal pattern of degeneration.

We use our models to determine if photoreceptor degeneration could spread due to hyperoxia; the conditions under which a degenerate patch of photoreceptors will remain stable and under which it will spread; which spatio-temporal patterns of progression are possible or most likely via this mode of degeneration; the variation in the wave speed of degeneration with eccentricity; and the effects of treatment with antioxidants and trophic factors, and of capillary loss upon photoreceptor degeneration.

The remainder of this paper is structured as follows: in Section 2 we develop the models, in Section 3 we suppose that the capillaries remain healthy and examine degenerate patch stability (Sections 3.1 and 3.2), the wave speed of degeneration (Sections 3.3 and 3.4), the effects of mutation-induced rod and/or cone loss (Sections 3.5 and 3.6), and the effects of treatment with antioxidants and trophic factors (Section 3.7). In Section 4 we consider the effects of capillary degeneration upon photoreceptor loss. Lastly, in Section 5 we discuss our results and suggest directions for future research.

2. Model Formulation

We view the posterior of the eye as a spherical cap and describe the geometry of the retina using spherical polar coordinates, (r, θ, ϕ), where θ is the polar angle and ϕ is the azimuthal angle (see Figure 1). Since the part of the eye containing the retina is almost spherical (Oyster, 1999) this is a reasonable approximation. The fovea lies almost exactly at the centre of the retina, opposite the lens, and so, ignoring the optic disc, we

assume that the retina is axisymmetric about the z-axis (oriented to pass outwards through the centre of the fovea, perpendicular to the wall of the eye) and neglect variation in the azimuthal angle, ϕ. We also neglect variation in the radial displacement, r, in order to form the simplest non-trivial model. This approximation is justified since the retinal width is approximately 10^4 times thinner than the retina's displacement from the origin and we are concerned only with its outer portion, between the photoreceptor ISs and the CC.

Having defined the geometry, we construct PDEs for the retinal oxygen concentration, $c(\theta, t)$, photoreceptor density, $p(\theta, t)$, and the capillary surface area per unit volume of tissue, $h(\theta, t)$. The oxygen equation reads:

$$\frac{\partial c}{\partial t} = \underbrace{\frac{D}{R^2 \sin(\theta)} \frac{\partial}{\partial \theta}\left(\sin(\theta)\frac{\partial c}{\partial \theta}\right)}_{\text{diffusion}} - \underbrace{\frac{\alpha Q p c}{\gamma + c}}_{\text{uptake}} + \underbrace{\beta h (c_{ch} - c)}_{\substack{\text{exchange with} \\ \text{choroid}}}, \tag{1}$$

where D is the diffusion coefficient and R is the radius of the retina. We use a Michaelis-Menten term for the rate of oxygen uptake, where the Michaelis constant, γ, is the oxygen concentration at which the rate of uptake is half maximal. The parameter Q represents the maximum rate of oxygen uptake per photoreceptor-containing tissue unit, achieved as $c \to \infty$. It is defined in terms of photoreceptor-containing tissue units, rather than simply photoreceptors, since the whole of the outer retina, from the ISs outward, is included in the model, including the OSs, which do not consume oxygen, and the RPE, which does. We assume that RPE degeneration occurs in tandem with photoreceptor loss, such that the rate of oxygen uptake is directly proportional to the local photoreceptor density, p. The parameter α is the ratio of unit surface area (per photoreceptor-containing tissue unit) to unit volume (per photoreceptor-containing tissue unit) and ensures dimensional consistency. We define c_{ch} as the oxygen concentration in the CC and β as the permeability of the CC vessels to oxygen.

The photoreceptor dynamics are given by the following equation

$$\frac{\partial p}{\partial t} = \underbrace{\mu p\left(1 - \frac{p}{\tilde{p}(\theta)}\right)\lambda_1(c)}_{\substack{\text{regrowth (normoxia)}}} - \underbrace{\delta p \lambda_2(c)}_{\substack{\text{degeneration} \\ \text{(hyperoxia)}}}. \tag{2}$$

We use a logistic regrowth term and an exponential decay term, where μ is the intrinsic growth rate and δ is the rate of hyperoxia-driven degeneration. The functions $\lambda_1(c)$ and $\lambda_2(c)$ are defined as follows:

$$\lambda_1(c) = 1 - H(c - c_{crit}), \qquad \lambda_2(c) = 1 - \lambda_1(c) = H(c - c_{crit}) = \begin{cases} 0 & \text{if } c < c_{crit}, \\ 1 & \text{if } c \geq c_{crit}, \end{cases} \tag{3}$$

where $H(c - c_{crit})$ is a Heaviside step function and c_{crit} is the *hyperoxic threshold*, below which oxygen levels are considered normoxic and above which they are considered hyperoxic. We assume that rods and cones have the same hyperoxic threshold. Therefore, under normoxia, $\lambda_1 = 1$, $\lambda_2 = 0$ and regrowth is active, whereas, under hyperoxia, $\lambda_1 = 0$, $\lambda_2 = 1$ and degeneration is active. The carrying capacity, $\tilde{p}(\theta)$, is the healthy photoreceptor profile, and is given by

$$\tilde{p}(\theta) = \underbrace{B_1 e^{-b_1\theta} + B_2 e^{-b_2\theta}}_{\text{Cones}} + \underbrace{B_3 \theta e^{-b_3\theta}}_{\text{Rods}}, \tag{4}$$

where B_1, B_2, B_3, b_1, b_2 and b_3 are positive constants. This phenomenological expression gives a good fit with the experimental profiles (see Figure 1(b) for a comparison between the fitted and experimental profiles and the Supplementary Material for details of the fitting procedure).

Before continuing we remark that, whilst the interpretation of $p(\theta, t)$ as photoreceptor density is consistent with the work presented throughout most of this paper, in which regrowth does not occur, it is inconsistent with the scenarios, considered in Sections 3.7 and 4.3, where regrowth occurs, since no new photoreceptors are generated following development. In this case, $p(\theta, t)$ should be interpreted as the OS biomass density (multiplied by an appropriate scaling factor to ensure dimensional consistency), since the photoreceptor OSs shrink to near zero length prior to the point at which irreversible photoreceptor damage is reached and can regrow once normoxia is restored (Chrysostomou et al., 2008; Lee et al., 2012; Milam et al., 1998). Here, photoreceptor oxygen demand is assumed to scale linearly with OS length, which indicates the health of the photoreceptor. We also assume that RPE oxygen consumption, which is small in comparison to that of the photoreceptors, scales linearly with OS length, since the rate of phagocytosis of shed OS tips, and the associated energy requirements, are diminished when the OS are short. This is implicit in the oxygen uptake term in equation (1).

The capillary dynamics are described by the following equation

$$\frac{\partial h}{\partial t} = \underbrace{\eta\left(\tilde{h}\frac{p}{\tilde{p}(\theta)} - h\right)}_{\substack{\text{degeneration} \\ \text{and regrowth}}}, \tag{5}$$

where η is the rate of capillary degeneration/regrowth and $\tilde{h}$ is the (constant) healthy capillary surface area per unit volume of tissue, that is, the value taken by $h(\theta, t)$ in the absence of degeneration. We assume that capillaries depend upon photoreceptors for survival (see Section 1). Since the mechanism is unknown, we choose an explicit relationship for simplicity. In particular, we assume that capillaries adapt to the local photoreceptor density, $p(\theta, t)$, such that they are maintained in the same proportion to $\tilde{h}$, as local photoreceptor density is to healthy photoreceptor density $\tilde{p}(\theta)$, that is, we would have $h(\theta, t)/\tilde{h} = p(\theta, t)/\tilde{p}(\theta)$, if $p(\theta, t)$ were maintained at steady-state. We do not use a logistic term in equation (5), since capillary regrowth is likely to emanate from healthy regions of the choroid that surround the degenerate patch, rather than from the patch itself.

We impose the following boundary and initial conditions to close equations (1), (2) and (5):

$$\frac{\partial c}{\partial \theta}(0, t) = 0 = \frac{\partial c}{\partial \theta}(\Theta, t), \tag{6}$$

$$c(\theta, 0) = c_{init}(\theta), \qquad p(\theta, 0) = p_{init}(\theta) = F(\theta)\tilde{p}(\theta), \qquad h(\theta, 0) = h_{init}(\theta) = G(\theta)\tilde{h}. \tag{7}$$

Zero-flux boundary conditions are justified by symmetry at the centre of the fovea ($\theta = 0$), whilst the retina terminates at the ora serrata ($\theta = \Theta$) indicating that zero-flux boundary conditions are appropriate here also. The (dimensionless) function $F(\theta)$ ($G(\theta)$) is either unity, or is unity everywhere except within an interval where it is zero, such that a patch of photoreceptors (capillaries) is removed. The initial oxygen distribution, $c_{init}(\theta)$, is the steady-state oxygen concentration corresponding to the initial photoreceptor and capillary profiles (that is, the steady-state solution to (1) and (6) with $p = p_{init}(\theta)$ and $h = h_{init}(\theta)$). See the Supplementary Material for dimensional model parameter values and justification of parameter choices.

2.1. Non-dimensionalisation

To simplify the subsequent analysis, we non-dimensionalise equations (1)–(7), scaling the independent and dependent variables, together with the initial conditions for oxygen and capillaries, as follows

$$\theta = \Theta\theta^*, \quad t = \frac{t^*}{\delta}, \quad c = c_{ch}c^*, \quad p = \tilde{p}_A p^*, \quad h = \tilde{h}h^*, \quad c_{init} = c_{ch}c^*_{init}, \quad h_{init} = \tilde{h}h^*_{init},$$

where $\tilde{p}_A$ is the mean photoreceptor density, such that the photoreceptor distribution is normalised. We scale time with the rate of hyperoxia-driven degeneration, δ, this being the timescale of interest. We define the following non-dimensional parameters:

$$D^* = \frac{D}{R^2\Theta^2\delta}, \quad Q^* = \frac{\alpha\tilde{p}_A}{c_{ch}\delta}Q, \quad \gamma^* = \frac{\gamma}{c_{ch}}, \quad \beta^* = \frac{\tilde{h}\beta}{\delta}, \quad c^*_{crit} = \frac{c_{crit}}{c_{ch}}, \quad \mu^* = \frac{\mu}{\delta}, \quad \eta^* = \frac{\eta}{\delta},$$

$$B^*_1 = \frac{B_1}{\tilde{p}_A}, \quad B^*_2 = \frac{B_2}{\tilde{p}_A}, \quad B^*_3 = \frac{\Theta B_3}{\tilde{p}_A}, \quad b^*_1 = \Theta b_1, \quad b^*_2 = \Theta b_2, \quad b^*_3 = \Theta b_3,$$

noting that $\lambda^*_1(c^*) = \lambda_1(c)$, $\lambda^*_2(c^*) = \lambda_2(c)$ and $\tilde{p}^*(\theta^*) = B^*_1 e^{-b^*_1\theta^*} + B^*_2 e^{-b^*_2\theta^*} + B^*_3\theta^* e^{-b^*_3\theta^*}$.

Since oxygen diffusion, uptake and production occur on much faster timescales (seconds) than the degeneration and regrowth of photoreceptors and capillaries (days–decades, see the dimensionless values of D, Q, β, μ and η in Table 1 and the dimensional values in Table S1), we assume that the oxygen concentration is at quasi-steady-state. Therefore, dropping the stars, equations (1), (2) and (5)–(7) reduce to

$$0 = \frac{D}{\sin(\Theta\theta)}\frac{\partial}{\partial\theta}\left(\sin(\Theta\theta)\frac{\partial c}{\partial\theta}\right) - \frac{Qpc}{\gamma + c} + \beta h(1 - c), \tag{8}$$

$$\frac{\partial p}{\partial t} = \mu p\left(1 - \frac{p}{\tilde{p}(\theta)}\right)\lambda_1(c) - p\lambda_2(c), \tag{9}$$

$$\frac{\partial h}{\partial t} = \eta\left(\frac{p}{\tilde{p}(\theta)} - h\right), \tag{10}$$

$$\frac{\partial c}{\partial\theta}(0, t) = 0 = \frac{\partial c}{\partial\theta}(1, t), \tag{11}$$

$$p(\theta, 0) = p_{init}(\theta) = F(\theta)\tilde{p}(\theta), \qquad h(\theta, 0) = h_{init}(\theta) = G(\theta), \tag{12}$$

where $\theta \in [0, 1]$. Table 1 summarises the non-dimensional parameter values. Each of the values in this table has either been taken from, fitted to or estimated from experimental data (subject to non-dimensionalisation), with the following exceptions. The parameters t_{crit} and c_{crit_2} are chosen to investigate the timing and strength of theoretical treatment regimes. The parameter μ is assumed to equal the rate of photoreceptor degeneration and is consistent with the timescale of photoreceptor OS regrowth. The value of η is unknown, so we conduct a sensitivity analysis to determine the significance of this parameter choice (see Section 4.3). Finally, we know that since the healthy retina does not undergo hyperoxia-driven photoreceptor degeneration and photoreceptors are sensitive to elevated oxygen concentrations, c_{crit} and c_{crit_1} must be higher than the maximum steady-state oxygen concentration under healthy conditions and lower than the level in the CC. The choice of c_{crit} and c_{crit_1} within this range does not affect the qualitative behaviour of the system. The dimensionless parameters in equation (8) span eight orders of magnitude, from $\gamma = O(10^{-2})$ to $Q, \beta = O(10^6)$. We exploit this separation of scales in Sections 3.2, 3.4 and 4.2, where we perform asymptotic analyses to determine the leading order behaviour of the system.

2.2. Mutation-induced Rod Degeneration

In the healthy human retina, mid-peripheral rods are lost throughout adult life, whilst cone numbers, and equatorial (halfway between the front and the back of the eye) and far-peripheral rod numbers, remain relatively stable (Curcio et al., 1993). In the RP retina, rods express mutant genes, increasing their vulnerability to apoptosis across the whole retina. We may incorporate hyperoxia-independent, mutation-induced rod degeneration into our model, in order to examine its effects upon the spatio-temporal pattern of photoreceptor loss.

Table 1: Parameters associated with the non-dimensional models (see equations (8)–(20)). See Section 2.1 for the relations between these dimensionless parameters and the dimensional parameters, Tables S1 and S2 for the sources of the dimensional parameters and Section S1 for a justification of parameter choices.

Parameter	Description	Value
D	Oxygen diffusion coefficient	77.7
Q	Maximum rate of oxygen uptake per photoreceptor-containing tissue unit	4.89×10^6
γ	Michaelis constant	1.67×10^{-2}
β	Capillary permeability	7.23×10^6
c_{crit}	Hyperoxic threshold	0.7
μ	Intrinsic growth rate of photoreceptors	1
η	Rate of CC degeneration/regrowth	10^{-4} to 10
B_1	Cone profile parameter	1.56
B_2	Cone profile parameter	0.158
B_3	Rod profile parameter	10.6
b_1	Cone profile parameter	71.8
b_2	Cone profile parameter	2.67
b_3	Rod profile parameter	3.06
ϕ_r	Rate of mutation-induced rod degeneration	6.6×10^{-3}
ϕ_c	Rate of mutation-induced cone degeneration	6.6×10^{-3}
t_{crit}	Time at which treatment is first applied	Various
c_{crit_1}	Hyperoxic threshold in the absence of treatment	0.7
c_{crit_2}	Boost to hyperoxic threshold resulting from treatment	0.1 or 0.3

In order to incorporate this second form of rod loss, we distinguish the rod and cone densities by $p_r(\theta, t)$ and $p_c(\theta, t)$ respectively. We replace equations (8)–(10) by the following dimensionless system:

$$0 = \frac{D}{\sin(\Theta\theta)} \frac{\partial}{\partial\theta} \left(\sin(\Theta\theta) \frac{\partial c}{\partial\theta} \right) - \frac{Q(p_r + p_c)c}{\gamma + c} + \beta h(1 - c), \tag{13}$$

$$\frac{\partial p_r}{\partial t} = -(\phi_r + \lambda_2(c))p_r, \tag{14}$$

$$\frac{\partial p_c}{\partial t} = \mu p_c \left(1 - \frac{p_c}{\tilde{p}_c(\theta)} \right) \lambda_1(c) - p_c \lambda_2(c), \tag{15}$$

$$\frac{\partial h}{\partial t} = \eta \left(\frac{p_r + p_c}{\tilde{p}_r(\theta) + \tilde{p}_c(\theta)} - h \right), \tag{16}$$

wherein

$$\tilde{p_r}(\theta) = B_3\theta e^{-b_3\theta}, \qquad \tilde{p_c}(\theta) = B_1 e^{-b_1\theta} + B_2 e^{-b_2\theta}, \tag{17}$$

are the healthy rod and cone profiles respectively. We do not include a logistic growth term in equation (14), assuming that the rods' mutant state compromises their ability to regenerate biomass. We also note that whilst the logistic growth term used in equation (15) is not strictly consistent with that used in equation (9), in that the sum of logistic growth terms for rods, p_r, and cones, p_c, is not the same as the logistic growth

term for photoreceptors, $p = p_r + p_c$, it remains the sensible choice, since we expect regeneration of cone biomass to obey saturation dynamics, such as logistic dynamics.

Following Clarke et al. (2000), we assume that mutation-induced rod degeneration is exponential, denoting its rate by ϕ_r, which we suppose to be constant across the domain, since RP affects all rods. For simplicity, and in the absence of further information, we also assume that the contributions of mutation and hyperoxia to rod degeneration combine in an additive fashion.

We close the system by imposing the following initial conditions:

$$p_r(\theta, 0) = p_{r_{init}}(\theta) = F(\theta)\tilde{p}_r(\theta), \qquad p_c(\theta, 0) = p_{c_{init}}(\theta) = F(\theta)\tilde{p}_c(\theta), \qquad h(\theta, 0) = h_{init}(\theta) = G(\theta), \tag{18}$$

together with the zero-flux oxygen boundary conditions given by equation (11) (see Table 1 for parameter values).

2.3. Mutation-induced Cone Degeneration

RP usually presents as a rod-cone dystrophy, in which rod loss precedes cone loss; however, RP sometimes presents as a cone-rod dystrophy, in which cone loss precedes rod loss (Hamel, 2006; Hartong et al., 2006). In this case, the underlying genetic mutation is more detrimental to cones than to rods.

The equations used to model cone-rod dystrophy are identical to those that model rod-cone dystrophy, except that equations (14)–(15) become:

$$\frac{\partial p_r}{\partial t} = \mu p_r \left(1 - \frac{p_r}{\tilde{p}_r(\theta)}\right) \lambda_1(c) - \lambda_2(c) p_r, \tag{19}$$

$$\frac{\partial p_c}{\partial t} = -(\phi_c + \lambda_2(c)) p_c, \tag{20}$$

so that the hyperoxia-independent mutation-induced degeneration term is now included in the cone equation, rather than the rod equation. Additionally, only rods, rather than cones, can regenerate biomass. The oxygen and capillary equations, together with the initial and boundary conditions, are given by equations (13), (16), (18) and (11) respectively (see Table 1 for parameter values).

2.4. Treatment with Antioxidants or Trophic Factors

Lastly, we consider the case in which treatment is applied in the form of either antioxidants or trophic factors. Antioxidants neutralise reactive oxygen species, whilst trophic factors increase photoreceptor resistance to apoptosis (Kohen and Nyska, 2002; Komeima et al., 2006, 2007; Yu et al., 2004). In either case, the treatments are assumed to increase the hyperoxic threshold, c_{crit}. Thus, to apply treatment, we set $c_{crit}(t) = c_{crit_1} + c_{crit_2} H(t - t_{crit})$, where c_{crit_1}, c_{crit_2} and t_{crit} are positive constants and $H(t - t_{crit})$ is a Heaviside step function, such that $H(t - t_{crit}) = 0$ for $t < t_{crit}$ and $H(t - t_{crit}) = 1$ for $t \geq t_{crit}$ (see Table 1 for parameter values).

3. Results: Model 1 — No Capillary Degeneration

In this section, we consider the dynamics of photoreceptor loss when capillary degeneration is neglected, i.e. the capillary surface area per unit volume of tissue is given by $h(\theta, t) \equiv 1$, rather than the dynamics summarised by equations (5), (10) and (16) for the respective models.

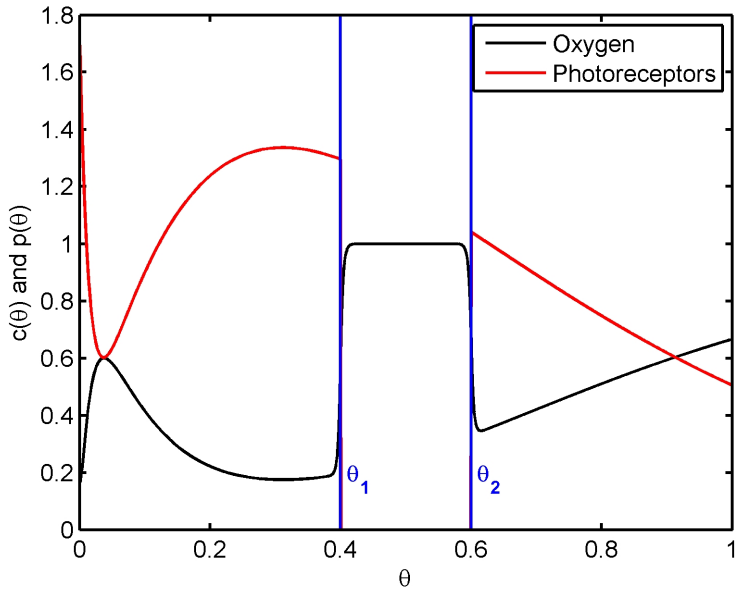

Figure 2: An example of the photoreceptor profile and associated oxygen profile when a patch of photoreceptors is removed. The vertical lines demarcate the boundaries of the degenerate patch. To obtain $c(\theta)$, equations (8) and (11) were solved using the finite difference method, with $p(\theta) = (H(\theta - \theta_2) + H(\theta_1 - \theta))\tilde{p}(\theta)$ and $h(\theta) = 1$. Parameter values: $\theta_1 = 0.4$ and $\theta_2 = 0.6$. Remaining parameter values as in Table 1.

3.1. Conditions for the Spread of Photoreceptor Degeneration: Numerical Solution to the Steady-state Problem

Since the initial loss of photoreceptors in humans typically occurs in patches, it is of interest to determine the conditions under which a patch of photoreceptor loss will enlarge over time. In what follows, a patch is said to be stable if it remains stationary and to be unstable if it expands. Similarly, a region of the retina is said to be stable if patch boundaries contained within it remain stationary, and unstable otherwise. Whilst this usage is non-standard, it serves as a convenient shorthand. In this section, and that which follows, we explore how the stability of a degenerate patch depends upon its width and the eccentricity of its end points, and how this relates to the (non-uniform) photoreceptor density profile. Since we are assuming axial symmetry, the patches considered here correspond to annuli in 2D.

To determine whether a degenerate patch will spread, we need only to consider equations (8) and (11), for fixed $p(\theta)$ and $h(\theta)$. We remove a patch of photoreceptors from the interval $\theta \in [\theta_1, \theta_2]$, where $0 \leq \theta_1 < \theta_2 \leq 1$, by setting $p(\theta) = F(\theta)\tilde{p}(\theta)$, where $F(\theta) = H(\theta - \theta_2) + H(\theta_1 - \theta)$, and fix the capillary surface area per unit volume of tissue at its healthy level, $h(\theta) = 1$ (we examine the effect of capillary loss on patch stability in Sections 4.1 and 4.2). As an example, Figure 2 shows the oxygen and photoreceptor profiles when $\theta_1 = 0.4$ and $\theta_2 = 0.6$. The oxygen profile rises sharply on the borders of the patch, reaching capillary levels within the patch. This sharp transition arises because the uptake and supply of oxygen, $Q = O(10^6)$ and $\beta = O(10^6)$, dominate over diffusion, $D = O(10^2)$ (see Table 1 for parameter values).

In order for a patch to spread, oxygen levels in the regions neighbouring the patch must be greater than or equal to the hyperoxic threshold, c_{crit}. This will occur if and only if $c(\theta_1) \geq c_{crit}$ and/or $c(\theta_2) \geq c_{crit}$.

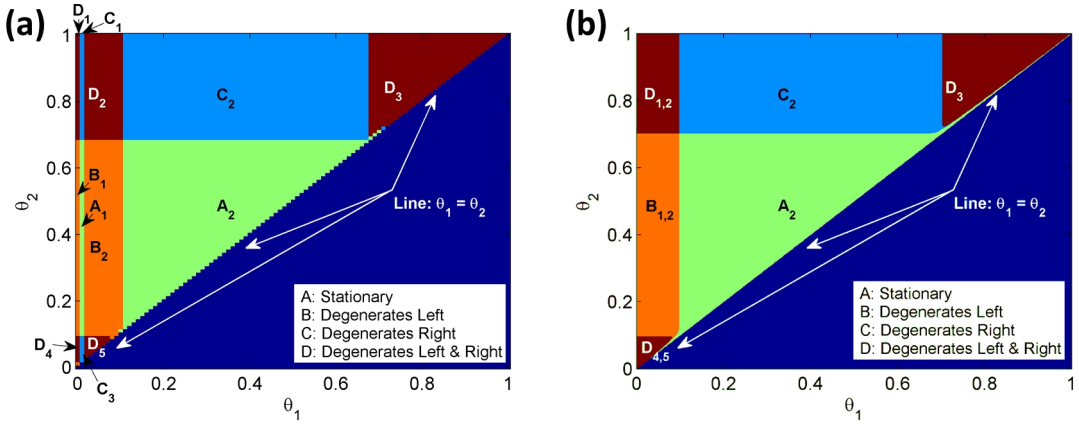

Figure 3: Diagrams to show the stable and unstable regions in (θ_1, θ_2) parameter space as revealed by numerical simulations and asymptotic analysis. (a) Equations (8) and (11) were solved using the finite difference method, with 10,001 mesh points, $p(\theta) = (H(\theta - \theta_2) + H(\theta_1 - \theta))\tilde{p}(\theta)$ and $h(\theta) = 1$, and (b) equations (33) and (34) were evaluated, for a range of values of both θ_1 and θ_2, where $\theta_1 < \theta_2$. If $c(\theta_i) < c_{crit}$, then the boundary at θ_i is stable; if $c(\theta_i) \geq c_{crit}$, then the boundary is unstable. Parameter values as in Table 1.

Therefore, by solving equations (8) and (11) for a range of values of θ_1 and θ_2, where $\theta_1 < \theta_2$, we may determine patch stability for a range of patch widths and locations.

We construct numerical solutions to equations (8) and (11) by discretising in space using the finite difference method and solving the resulting system of nonlinear algebraic equations using the Matlab routine fsolve, employing the Trust-Region-Dogleg algorithm.

Figure 3(a) summarises the results of our numerical simulations: (θ_1, θ_2) parameter space is decomposed into distinct regions, characterised by the oxygen distribution associated with the removal of the relevant patch. Depending upon the positions of its endpoints, a patch may either remain stationary (regions A_1 and A_2), degenerate to the left (regions B_1 and B_2), degenerate to the right (regions C_1–C_3) or degenerate to both the left and right (regions D_1–D_5). These results show that, in general, it is the position of the endpoints of a patch, rather than its width, that determines its stability properties. The analysis in the next section enables us to explain and expand upon these results.

3.2. *Conditions for the Spread of Photoreceptor Degeneration: Mathematical Analysis of the Steady-state Problem*

We use asymptotic analysis to derive leading order analytical expressions for the oxygen concentration on the boundaries of a degenerate patch, and hence to determine its stability properties. As before, we take $h(\theta) = 1$ and note that, since we are dealing with the steady-state problem, $c = c(\theta)$ and $p = p(\theta)$.

We begin by scaling the non-dimensional model parameters so that they are all of $O(1)$. Choosing $\epsilon = O(10^{-2})$, we scale: $D = \epsilon^{-1}D'$, $Q = \epsilon^{-3}Q'$, $\gamma = \epsilon\gamma'$, $\beta = \epsilon^{-3}\beta'$ and $b_1 = \epsilon^{-1}b_1'$. We have chosen ϵ to provide a clear separation between the magnitudes of the parameters. Dropping the dashes, equation (8) yields the following singular ODE for $c = c(\theta)$:

$$0 = \epsilon^2 D\frac{\mathrm{d}^2c}{\mathrm{d}\theta^2} + \epsilon^2 D\Theta\cot(\Theta\theta)\frac{\mathrm{d}c}{\mathrm{d}\theta} - \frac{Qp(\theta)c}{\epsilon\gamma + c} + \beta(1 - c), \tag{21}$$

where $p(\theta) = F(\theta)\tilde{p}(\theta)$ is the instantaneous photoreceptor distribution, and

$$\tilde{p}(\theta) = B_1 e^{-\epsilon^{-1} b_1 \theta} + B_2 e^{-b_2 \theta} + B_3 \theta e^{-b_3 \theta}. \tag{22}$$

As before, we impose zero-flux boundary conditions, so that

$$\frac{\mathrm{d}c}{\mathrm{d}\theta}(0) = 0 = \frac{\mathrm{d}c}{\mathrm{d}\theta}(1). \tag{23}$$

We form the regular perturbation expansions:

$$c(\theta) = c_0(\theta) + \epsilon c_1(\theta) + O(\epsilon^2), \qquad p(\theta) = p_0(\theta) + \epsilon p_1(\theta) + O(\epsilon^2), \tag{24}$$

noting that $(\epsilon\gamma + c)^{-1} = c_0^{-1} - \epsilon(c_1 + \gamma)c_0^{-2} + O(\epsilon^2)$, and $\cot(\Theta\theta) \leq O(1)$ for $\theta \in (0.1, 1]$.

We define an isolated degenerate patch, such that $p(\theta) = F(\theta)\tilde{p}(\theta)$, where $F(\theta) = H(\theta - \theta_2) + H(\theta_1 - \theta)$ for $0.1 < \theta_1 < \theta_2 < 1 - \omega\epsilon$, where ω is a positive constant of $O(1)$. By bounding θ_1 and θ_2 in this way, we avoid the region $\theta \in [0, 0.1)$, in which $\cot(\Theta\theta) > O(1)$, together with the width $O(\epsilon)$ boundary layers at $\theta = 0$ and 1. The retinal geometry ensures that $\theta_2 - \theta_1 \leq O(1)$. We note that the case where $\theta_2 - \theta_1 = O(\epsilon)$ matches well with the patch widths measured in the rat by García-Ayuso et al. (2013); Ji et al. (2012); Zhu et al. (2013), which lie in the (non-dimensional) range 3.8×10^{-3}–1.9×10^{-2}.

We decompose the domain into outer and inner regions. In the outer regions, the oxygen profile varies gradually with eccentricity, whilst, in the inner regions, it typically varies rapidly with eccentricity. We construct leading order solutions at the patch boundaries, using the boundary conditions and asymptotic matching to determine the constants of integration (Bender and Orszag, 1999).

The domain is partitioned as shown in Figure 4. The discontinuities in $p(\theta)$ at $\theta = \theta_1$ and $\theta = \theta_2$ divide the domain into left, centre-inner and right regions. These discontinuities in $p(\theta)$ produce a discontinuous term in equation (21). As a result, we cannot use standard matching techniques to construct a solution which is valid across the whole domain. Instead, we use patching at these points, imposing continuity of the concentration and flux of oxygen (Bender and Orszag, 1999). The left and right regions are further subdivided into inner and outer regions — left-left-inner, left-outer and right-left-inner in the left region, and left-right-inner, right-outer and right-right-inner in the right region — to allow us to satisfy the boundary conditions at $\theta = 0$, θ_1, θ_2 and 1 (though we do not need to deal with the $\theta = 0$ or 1 boundaries here, as this is not required to find leading order solutions at $\theta = \theta_1$ and θ_2).

In the left-outer and right-outer regions, equation (22) supplies $p_0(\theta) = K(\theta)$, where $K(\theta) := B_2 e^{-b_2\theta} + B_3\theta e^{-b_3\theta}$, whilst equation (21) yields

$$c_0(\theta) = 1 - \frac{Q}{\beta} K(\theta). \tag{25}$$

In the right-left- and centre-inner regions we rescale $\hat{\theta} = \epsilon^{-1}(\theta - \theta_1)$, in order to achieve a dominant balance between the diffusion term and kinetic terms in equation (21), yielding

$$0 = D\frac{\mathrm{d}^2 c}{\mathrm{d}\hat{\theta}^2} + \epsilon D\Theta \cot(\Theta(\theta_1 + \epsilon\hat{\theta}))\frac{\mathrm{d}c}{\mathrm{d}\hat{\theta}} - \frac{Qp(\hat{\theta})c}{\epsilon\gamma + c} + \beta(1 - c). \tag{26}$$

In the right-left-inner region, equation (22) supplies $p_0(\hat{\theta}) = K(\theta_1)$, which is constant. Therefore, at leading order, equation (26) yields

$$c_0(\hat{\theta}) = 1 - \frac{Q}{\beta} K(\theta_1) + A_1 e^{\sqrt{\frac{\beta}{D}}\hat{\theta}} + A_2 e^{-\sqrt{\frac{\beta}{D}}\hat{\theta}}, \tag{27}$$

where the A_is in this equation, and those that follow, are constants.

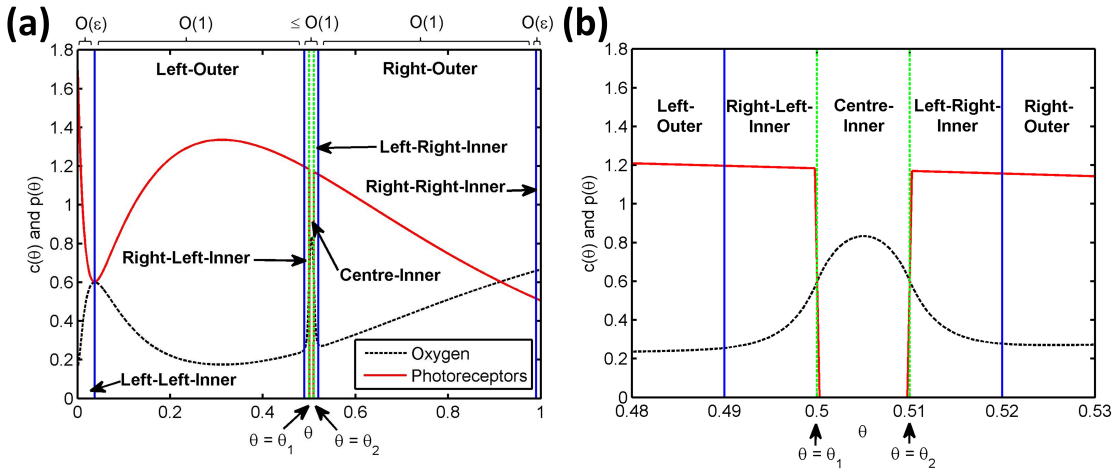

Figure 4: Diagrams to show the locations of the outer and inner regions for the case of a narrow degenerate patch. The full domain is shown in (a), while (b) magnifies the region from which photoreceptors have been removed. The solid vertical lines demarcate the approximate limits of the boundary layers, whilst the dashed vertical lines mark the positions of θ_1 and θ_2. To obtain $c(\theta)$, equations (8) and (11) were solved using the finite difference method, where $p(\theta) = (H(\theta - \theta_2) + H(\theta_1 - \theta))\tilde{p}(\theta)$ and $h(\theta) = 1$. Parameter values: $\theta_1 = 0.5$ and $\theta_2 = 0.51$. Remaining parameter values as in Table 1.

In the centre-inner region, $p_0(\hat{\theta}) = 0$ and equation (26) yields

$$c_0(\hat{\theta}) = 1 + A_3 e^{\sqrt{\frac{\beta}{D}}\hat{\theta}} + A_4 e^{-\sqrt{\frac{\beta}{D}}\hat{\theta}}. \tag{28}$$

In the left-right-inner region we rescale $\bar{\theta} = \epsilon^{-1}(\theta - \theta_2)$, in order to achieve a dominant balance between the diffusion term and kinetic terms in equation (21), yielding an equation equivalent to equation (26), where $\hat{\theta} \mapsto \bar{\theta}$ and $\theta_1 \mapsto \theta_2$. In this region, equation (22) supplies $p_0(\bar{\theta}) = K(\theta_2)$, which is constant, and we obtain

$$c_0(\bar{\theta}) = 1 - \frac{Q}{\beta}K(\theta_2) + A_5 e^{\sqrt{\frac{\beta}{D}}\bar{\theta}} + A_6 e^{-\sqrt{\frac{\beta}{D}}\bar{\theta}}. \tag{29}$$

It remains to determine the constants A_i ($i = 1,\ldots, 6$) using matching and imposing the relevant boundary conditions.

We begin by matching the left-outer and right-left-inner solutions using Van Dyke's matching rule, which states that the m term inner expansion of the n term outer solution, should equal the n term outer expansion of the m term inner solution. In this case we take both $m = 1$ and $n = 1$, since we are dealing with leading order solutions only. The 1 term (right-left-) inner expansion of the 1 term (left-) outer solution, (25), is

$$c(\hat{\theta}) \sim 1 - \frac{Q}{\beta}K(\theta_1).$$

Expanding equation (27) in (left-) outer variables we obtain

$$c(\theta) \sim 1 - \frac{Q}{\beta}K(\theta_1) + A_1 e^{-\epsilon^{-1}\sqrt{\frac{\beta}{D}}(\theta_1 - \theta)} + A_2 e^{\epsilon^{-1}\sqrt{\frac{\beta}{D}}(\theta_1 - \theta)}.$$

Since $(\theta_1 - \theta) > 0$, the third term is exponentially small, and may be neglected. However, the last term is exponentially large. Therefore, in order for the left-outer and right-left-inner solutions to match, we must have $A_2 = 0$. Matching the right-outer and left-right-inner regions in the same way, we find that $A_5 = 0$.

Patching together the right-left-inner, centre-inner and left-right-inner solutions, by imposing continuity in the concentration and flux of oxygen at $\theta = \theta_1$ and $\theta = \theta_2$, we obtain expressions for the remaining unknowns (A_1, A_3, A_4 and A_6) in terms of known parameters.

Substituting for A_i ($i = 1,\ldots, 6$) into equations (27)–(29), yields the right-left-inner solution

$$c_0(\theta) = 1 - \frac{Q}{2\beta}\left(K(\theta_1)\left(2 - e^{-\epsilon^{-1}\sqrt{\frac{\beta}{D}}(\theta_1-\theta)}\right) + K(\theta_2)e^{-\epsilon^{-1}\sqrt{\frac{\beta}{D}}(\theta_2-\theta)}\right), \tag{30}$$

the centre-inner solution

$$c_0(\theta) = 1 - \frac{Q}{2\beta}\left(K(\theta_1)e^{-\epsilon^{-1}\sqrt{\frac{\beta}{D}}(\theta-\theta_1)} + K(\theta_2)e^{-\epsilon^{-1}\sqrt{\frac{\beta}{D}}(\theta_2-\theta)}\right), \tag{31}$$

and the left-right-inner solution

$$c_0(\theta) = 1 - \frac{Q}{2\beta}\left(K(\theta_1)e^{-\epsilon^{-1}\sqrt{\frac{\beta}{D}}(\theta-\theta_1)} + K(\theta_2)\left(2 - e^{-\epsilon^{-1}\sqrt{\frac{\beta}{D}}(\theta-\theta_2)}\right)\right). \tag{32}$$

By substituting $\theta = \theta_1$ into either of equations (30) or (31), and by substituting $\theta = \theta_2$ into either of equations (31) or (32), we may derive the following expressions for the oxygen concentration at the left- and right-hand ends of the degenerate patch respectively:

$$c_0(\theta_1) = 1 - \frac{Q}{2\beta}\left(K(\theta_1) + K(\theta_2)e^{-\epsilon^{-1}\sqrt{\frac{\beta}{D}}(\theta_2-\theta_1)}\right), \tag{33}$$

$$c_0(\theta_2) = 1 - \frac{Q}{2\beta}\left(K(\theta_1)e^{-\epsilon^{-1}\sqrt{\frac{\beta}{D}}(\theta_2-\theta_1)} + K(\theta_2)\right). \tag{34}$$

When $(\theta_2 - \theta_1) \leq O(\epsilon)$, the oxygen concentration at the left- (right-) hand edge of the degenerate patch $c(\theta_1)$ ($c(\theta_2)$) depends upon the positions of the left- and right-hand ends of the patch $\theta = \theta_1$ and $\theta = \theta_2$. However, as $(\theta_2 - \theta_1)$ increases in magnitude to $O(1)$, the $e^{-\epsilon^{-1}\sqrt{\frac{\beta}{D}}(\theta_2-\theta_1)}$ terms become exponentially small, and equations (33) and (34) reduce to

$$c_0(\theta_i) = 1 - \frac{Q}{2\beta}K(\theta_i) \qquad (i = 1, 2), \tag{35}$$

at leading order. In this case the oxygen concentration at the edge of a patch is independent of the position of the other edge. An expression identical to equation (35) can be obtained if we begin our analysis by assuming that the degenerate patch is of width $O(1)$. In this case it is necessary to subdivide the centre-inner region into left-centre-inner, centre-outer and right-centre-inner regions (see Roberts, 2015, Chapter 4, for details). Therefore, the analysis presented in this section is valid for degenerate patches of width $0 \leq \theta_2 - \theta_1 \leq O(1)$.

In Figure 5 we use equation (35) to plot $c_0(\theta_i)$ for $\theta_i \in [0, 1]$ and observe that for $\theta_i \in (\theta_{crit_1}, \theta_{crit_2})$, $c < c_{crit}$, and $c \geq c_{crit}$ otherwise. Therefore, the degenerate patch will remain stationary provided both ends lie in the interval $(\theta_{crit_1}, \theta_{crit_2})$, henceforth known as the 'mid-peripheral stable region'. However, if one of its ends lies in one of the 'unstable regions' outside this interval, then it will move outwards, enlarging the patch. We label the left unstable region the 'para/perifoveal unstable region' and the right unstable region the 'peripheral unstable region'.

Inspection of equation (35) and Figure 5 reveals that the width of the mid-peripheral stable region increases as Q, B_2, B_3 or c_{crit} are increased and decreases as β, b_2 or b_3 are increased. It has been shown that rod density decreases with age in healthy individuals (Curcio et al., 1993), an effect which is exacerbated by RP. As rods are lost, B_3 and hence the width of the mid-peripheral stable region will decrease, which

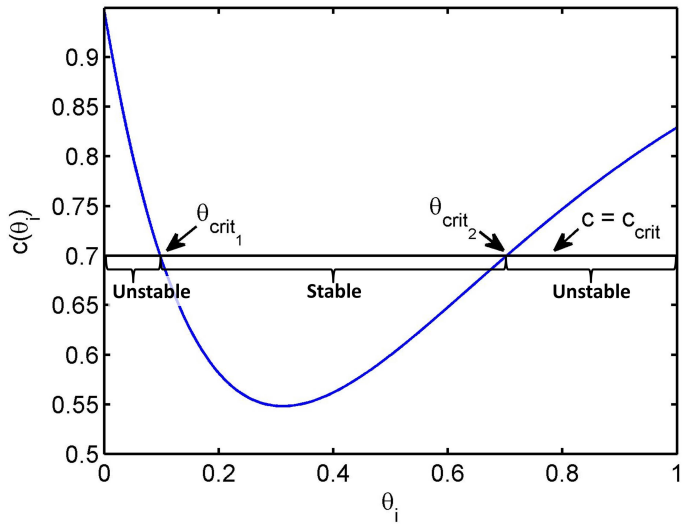

Figure 5: Variation of the oxygen concentration on the edge of a degenerate patch with eccentricity of the edge. Equation (35) is plotted using parameter values from Table 1 and the scalings described in Section 3.2. The horizontal line marks the hyperoxic threshold, on which $c = c_{crit}$. The positions of the endpoints of the stable region, $\theta = \theta_{crit_1}$ and $\theta = \theta_{crit_2}$, are defined implicitly via equation (36).

may destabilise previously stable degenerate patches, causing them to spread. We explore this possibility in Section 3.5.

An implicit equation for the boundaries of the mid-peripheral stable region, θ_{crit_1} and θ_{crit_2}, can be derived by setting $c_0(\theta_i) = c_{crit}$ in equation (35) to yield

$$0 = (1 - c_{crit}) - \frac{Q}{2\beta} K(\theta_{crit_i}) \qquad (i = 1, 2). \tag{36}$$

As can be seen from Figure 5, this equation has two roots in the interval $\theta_i \in [0, 1]$, the smaller of which corresponds to θ_{crit_1} and the larger of which corresponds to θ_{crit_2}.

Since the oxygen concentration at the left-hand boundary depends upon the position of the right-hand boundary and vice-versa in equations (33) and (34), the expressions that could be derived for the boundaries of the mid-peripheral stable region (by setting $c = c_{crit}$ in these equations, to yield expressions equivalent to (36)) are not particularly instructive. Instead, we may use equations (33) and (34) to determine the regions in (θ_1, θ_2) parameter space in which the patch is stable and unstable (see Figure 3(b)). The extension of region A_2 to the right of regions B_2, C_2, D_3 and D_5 is seen more clearly here than in the coarser numerical result. This demonstrates that degenerate patches can remain stable when one or both boundaries lie in regions that would render wide ($O(1)$ in width) patches unstable, provided they are sufficiently narrow ($\leq O(\epsilon)$ in width).

Figure 3(b) matches closely with the numerical solution in Figure 3(a), except that Regions A_1, C_1 and C_3 are absent from Figure 3(b). This is because, as noted above, the analysis presented in this section breaks down where $\theta_1 < 0.1$. The numerical results presented in Figure 3(a) demonstrate the existence of a second stable region, $(\theta_{crit_3}, \theta_{crit_4})$, within the para/perifoveal unstable region $[0, \theta_{crit_1}]$, in which the left-hand (and right-hand for sufficiently narrow patches) boundary of the patch remains stationary. We label the new stable region the 'near-central stable region', and the unstable region in which $\theta_c \leq \theta_{crit_3}$, the 'central

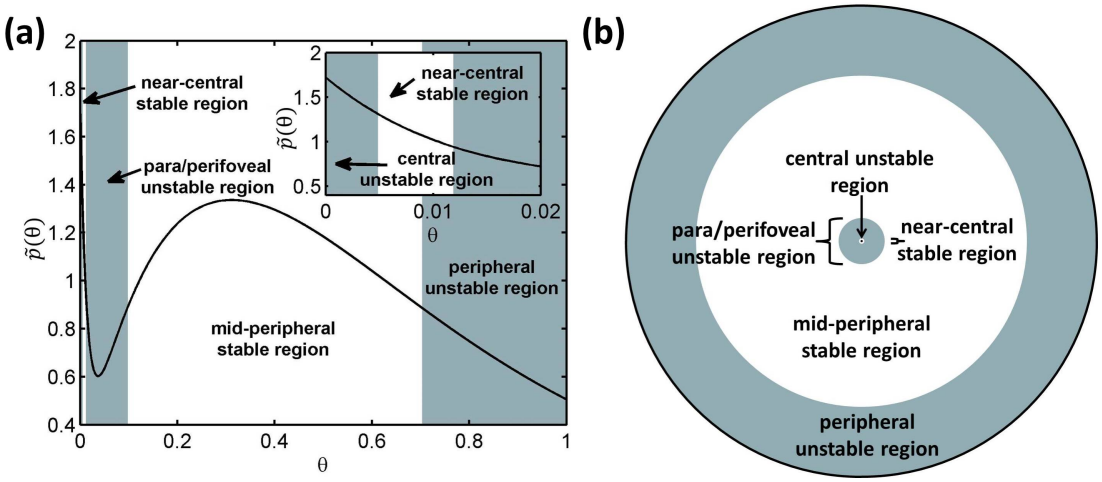

Figure 6: Diagrams to show the locations of the stable and unstable regions within the retina. Diagram (a) shows the relationship between the healthy photoreceptor profile and the stability regions in 1D, whilst (b) shows the locations of the stability regions in 2D. The central unstable region, which is extremely narrow, can be seen in the inset in (a).

unstable region'. Thus, the retina is sub-divided into 5 regions, as described in Figure 6.

3.3. Numerical Solution to the Time-dependent Problem

Having examined degenerate patch stability at steady-state, we now test our predictions (numerically) using the full dynamic model. We solve equations (8), (9), (11) and (12), with $h(\theta, t) = 1$, using the method of lines, discretising in space as for the steady-state problem, and integrating in time using an explicit Runge-Kutta method (Matlab routine ode45). The quasi-steady oxygen equation (equation (8)) is solved at each time step using fsolve, as for the steady-state problem considered earlier. We use 4001 mesh points in all simulations, so that the distance between mesh points corresponds to the average width of a photoreceptor. As a result, degeneration will spread only if the hyperoxic region extends by a photoreceptor width or more beyond the degenerate patch, ensuring the results are biologically realistic. We run all simulations to time $t = 200$ (dimensionless units) or until the system reaches steady-state, whichever occurs first. We choose $t = 200$ since this corresponds to just over 60 years, the natural time span of the disease following the initial loss of photoreceptors.

In Figure 7 we present simulation results for the time-dependent problem, with initial conditions selected from each type of region in Figure 3(a). In each case the solutions behave as predicted by the steady-state model. These simulations reveal that, once degeneration initiates, the speed of the wave of degeneration varies with eccentricity, being slower in regions with higher photoreceptor densities and faster in regions with lower densities. In the stable regions, photoreceptor density is too high to permit the spread of degeneration.

3.4. Travelling Wave Analysis

We use travelling wave analysis to derive an analytical expression for the wave speed of photoreceptor degeneration. Starting with equations (8) and (9), we relax the quasi-steady-state assumption on the oxygen

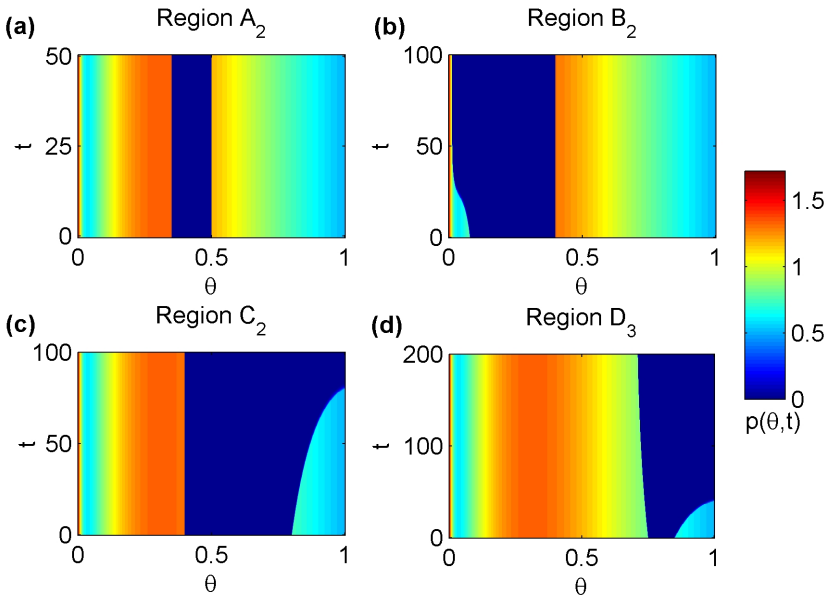

Figure 7: Dynamic simulations of photoreceptor loss and preservation, for a range of initial degenerate patch locations (θ_1, θ_2). In all cases the pattern of degeneration proceeds in a manner consistent with Figure 3(a). Equations (8), (9), (11) and (12) were solved using the method of lines, with 4001 mesh points, $h(\theta, t) = 1$ and $F(\theta) = H(\theta - \theta_2) + H(\theta_1 - \theta)$. Parameter values: (a) $(\theta_1, \theta_2) = (0.35, 0.50)$, (b) $(\theta_1, \theta_2) = (0.08, 0.40)$, (c) $(\theta_1, \theta_2) = (0.40, 0.80)$ and (d) $(\theta_1, \theta_2) = (0.75, 0.85)$. Remaining parameter values as in Table 1.

concentration, yielding

$$\frac{\partial c}{\partial t} = \frac{D}{\sin(\Theta\theta)}\frac{\partial}{\partial \theta}\left(\sin(\Theta\theta)\frac{\partial c}{\partial \theta}\right) - \frac{Qpc}{\gamma + c} + \beta(1-c), \tag{37}$$

$$\frac{\partial p}{\partial t} = \mu p\left(1 - \frac{p}{\tilde{p}(\theta)}\right)\lambda_1(c) - p\lambda_2(c), \tag{38}$$

where $h(\theta, t) = 1$.

Without loss of generality, we consider a wave of degeneration which travels in the direction of increasing θ, at speed v, such that photoreceptors are healthy ahead of the wave (to the right) and have degenerated behind the wave (to the left).

We transform to travelling wave coordinates $(\theta, t) \mapsto y = \theta - vt$. It can be seen from Figure 7 that $v = O(\epsilon)$. Therefore, adopting the asymptotic scalings used in Section 3.2, we also scale $v = \epsilon v'$, so that, upon dropping the dashes, we obtain

$$-\epsilon^4 v\frac{\mathrm{d}c}{\mathrm{d}y} = \frac{\epsilon^2 D}{\sin(\Theta(y+\epsilon vt))}\frac{\mathrm{d}}{\mathrm{d}y}\left(\sin(\Theta(y+\epsilon vt))\frac{\mathrm{d}c}{\mathrm{d}y}\right) - \frac{Qpc}{\epsilon\gamma + c} + \beta(1-c), \tag{39}$$

$$\epsilon v\frac{\mathrm{d}p}{\mathrm{d}y} = p\lambda_2(c) - \mu p\left(1 - \frac{p}{\tilde{p}(y+\epsilon vt)}\right)\lambda_1(c). \tag{40}$$

We remark that, in practice, the wave of degeneration is not an exact travelling wave, since its shape and speed vary over time with the local photoreceptor density. However, since the wavefront of the oxygen concentration, $c(y)$, is narrow (width $O(\epsilon)$), the photoreceptor density and wavefront shape are approximately locally constant. In what follows, we also treat the wave speed, v, as locally constant, noting that, when viewed over the full domain, it has a θ dependence contingent upon $\tilde{p} = \tilde{p}(\theta)$. We note that, unlike in Section 3.2, this analysis is valid in the region $\epsilon \lesssim \theta < 0.1$, provided the wave is travelling rightwards, and also provides a good approximation for the wave speed of leftward degeneration (see Figure 9(c)).

Since equation (40) is discontinuous at $y = y_{crit}$, where $c(y_{crit}) = c_{crit}$, we partition the domain into left-outer, left-inner, right-inner and right-outer regions, as shown in Figure 8. Seeking leading order solutions to equations (39) and (40), we find that $p_0(y) = 0$ and $c_0(y) = 1$ in the left-outer region, whilst in the right-outer region, $p_0(y) = \tilde{p}(y)$ and $c_0(y) = 1 - \frac{Q}{\beta}\tilde{p}(y)$. In the left- and right-inner regions we rescale $\bar{y}^* = \epsilon^{-1}(y - y_{crit})$, in order to achieve a dominant balance between the diffusion and kinetic terms in equation (39). Dropping the bars and stars, equations (39) and (40) become

$$-\epsilon^3 v\frac{\mathrm{d}c}{\mathrm{d}y} = D\frac{\mathrm{d}^2 c}{\mathrm{d}y^2} + \epsilon D\Theta\cot(\Theta(y_{crit} + \epsilon(y+vt)))\frac{\mathrm{d}c}{\mathrm{d}y} - \frac{Qpc}{\epsilon\gamma + c} + \beta(1-c), \tag{41}$$

$$v\frac{\mathrm{d}p}{\mathrm{d}y} = p\lambda_2(c) - \mu p\left(1 - \frac{p}{\tilde{p}(y_{crit} + \epsilon(y+vt))}\right)\lambda_1(c). \tag{42}$$

In the left-inner region equation (42) supplies $p_0(y) = A_7 e^{y/v}$, whilst equation (41) yields

$$c_0(y) = 1 + A_7\frac{Qv^2}{D - \beta v^2}e^{\frac{y}{v}} + A_8 e^{\sqrt{\frac{\beta}{D}}y} + A_9 e^{-\sqrt{\frac{\beta}{D}}y}, \tag{43}$$

where the A_is in these equations, and those that follow, are constants. Equation (43) holds for all v, except $v = \sqrt{D/\beta}$. In this case, the second term in equation (43) should be replaced by $A_7 Qvye^{y/v}/(2D)$. It can be shown, using matching and patching as below, that this case only arises when $\tilde{p} = 4\beta(1 - c_{crit})/(3Q)$, where $\tilde{p} = \tilde{p}(y_{crit})$ both here and in what follows.

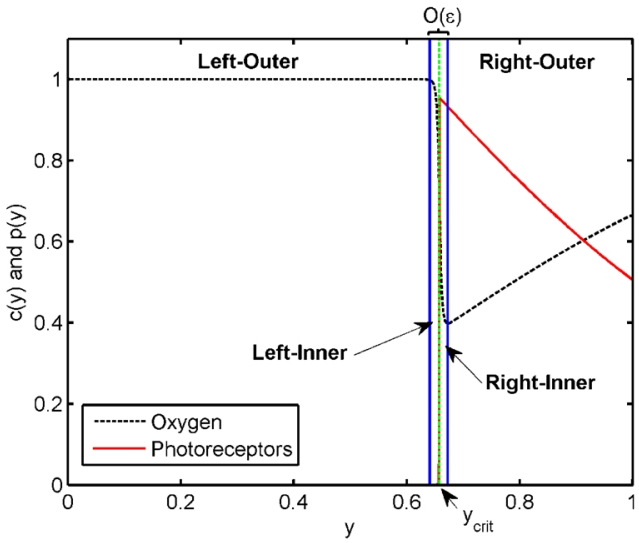

Figure 8: Diagram to show the locations of the outer and inner regions for the travelling wave analysis. The diagram shows the instantaneous oxygen and photoreceptor profiles from a dynamic simulation, such as those in Figure 7. The wave of degeneration is travelling to the right at speed v, in the (θ, t) frame. The solid vertical lines demarcate the approximate limits of the boundary layers, whilst the dashed vertical line marks the position of y_{crit}. See Table 1 for parameter values.

Henceforth, we assume that $v \neq \sqrt{D/\beta}$. In the right-inner region equation (42) supplies $p_0(y) = \tilde{p}$ (the right-inner boundary layer applying only to the oxygen concentration), whilst equation (41) yields

$$c_0(y) = 1 - \frac{Q}{\beta}\tilde{p} + A_{10}e^{\sqrt{\frac{\beta}{D}}y} + A_{11}e^{-\sqrt{\frac{\beta}{D}}y}. \tag{44}$$

Matching the left-outer and left-inner solutions, and the right-outer and right-inner solutions using Van Dyke's matching rule, as in Section 3.2, we find $A_9 = 0 = A_{10}$. Imposing continuity of $p_0(y)$ at $y = y_{crit}$ and ensuring that $c_0^-(y_{crit}) = c_{crit} = c_0^+(y_{crit})$ (where '−' and '+' denote left- and right-inner solutions respectively), yields 3 simultaneous equations for A_7, A_8 and A_{11} in terms of the model parameters. Rewriting equations (43) and (44) in outer variables, yields the left-inner solution

$$c_0(y) = 1 - \left(1 - c_{crit} + \frac{Qv^2}{D - \beta v^2}\tilde{p}\right)e^{-\epsilon^{-1}\sqrt{\frac{\beta}{D}}(y_{crit}-y)} + \frac{Qv^2}{D - \beta v^2}\tilde{p}e^{-\epsilon^{-1}\frac{(y_{crit}-y)}{v}}, \tag{45}$$

where $p_0(y) = \tilde{p}\exp(-\epsilon^{-1}(y_{crit} - y)/v)$, and the right-inner solution

$$c_0(y) = 1 - \frac{Q}{\beta}\tilde{p} - \left(1 - c_{crit} - \frac{Q}{\beta}\tilde{p}\right)e^{-\epsilon^{-1}\sqrt{\frac{\beta}{D}}(y-y_{crit})}, \tag{46}$$

where $p_0(y) = \tilde{p}$.

Lastly, imposing continuity of oxygen flux at $y = y_{crit}$ yields a quadratic equation for the wave speed, v, with roots v_+ and v_-. The larger root, $v_+ = \sqrt{D/\beta}$ must be rejected, since we assumed above that $v \neq \sqrt{D/\beta}$, whilst the smaller root supplies

$$v = \sqrt{\frac{D}{\beta}}\frac{2\beta(1 - c_{crit}) - Q\tilde{p}}{2(Q\tilde{p} - \beta(1 - c_{crit}))}. \tag{47}$$

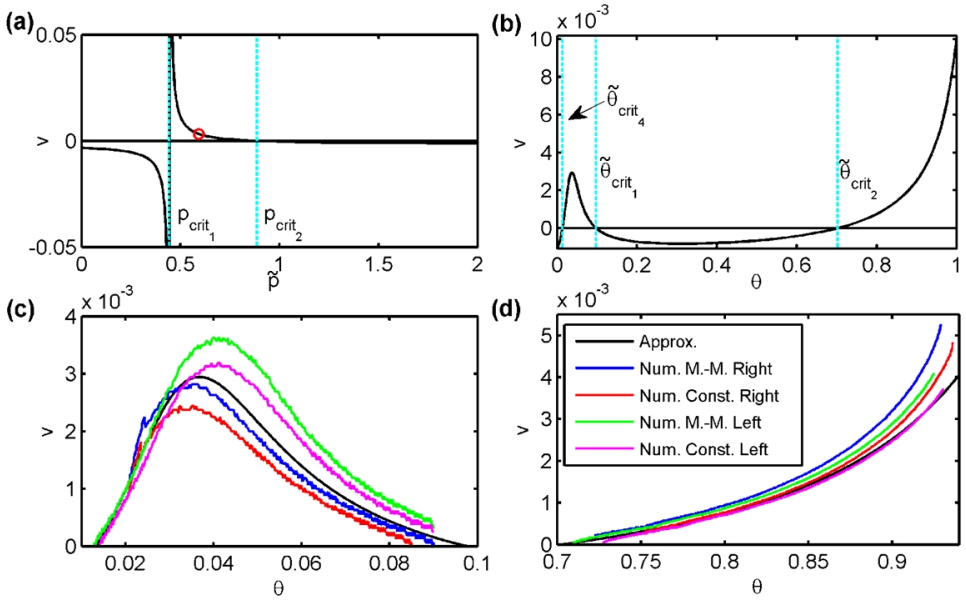

Figure 9: Graphs to show the dependence of the travelling wave speed upon the local photoreceptor density and retinal eccentricity. (a) Variation in wave speed with photoreceptor density. The wave of degeneration will only propagate where $v > 0$, that is where $p_{crit_1} < \tilde{p} < p_{crit_2}$ (demarcated by dashed vertical lines). Within this region the wave speed is a monotone decreasing function of the photoreceptor density. The circle marks the point $(\tilde{p}, v) = (4\beta(1 - c_{crit})/(3Q), \sqrt{D/\beta})$. (b) Variation in wave speed with eccentricity across the retina. The wave speed $v > 0$ for $\tilde{\theta}_{crit_4} < \theta < \tilde{\theta}_{crit_1}$ and $\theta > \tilde{\theta}_{crit_2}$. (c)–(d) Comparison of analytical and numerical wave speeds. Numerical results are shown for both Michaelis-Menten ($Qpc/(\gamma + c)$) and constant (Qp) oxygen uptake, and for rightward and leftward travelling waves. The numerical and analytical results are in good agreement. The legend in panel (d) applies to all four graphs. (a)–(d) The analytical wave speed is given by equation (47). (c)–(d) The numerical wave speeds were generated by solving equations (8), (9), (11) and (12) using the method of lines, with 4001 mesh points, $h(\theta, t) = 1$, $F(\theta) = H(\theta - \theta_2) + H(\theta_1 - \theta)$ and with modifications to the oxygen uptake term as described above (see text for further details). See Table 1 for parameter values.

This equation is independent of the scaling with respect to ϵ (that is, it remains unchanged if we revert to the undashed parameters: $D = \epsilon^{-1}D'$, $Q = \epsilon^{-3}Q'$, $\beta = \epsilon^{-3}\beta'$ and $v = \epsilon v'$). Inspection of equation (47) reveals that v is a monotone decreasing function of $\tilde{p}$, where $v > 0$ for $p_{crit_1} < \tilde{p} < p_{crit_2}$, $v = 0$ when $\tilde{p} = p_{crit_2} = 2\beta(1 - c_{crit})/Q$, and $v \to \infty$ as $\tilde{p} \downarrow p_{crit_1} = \beta(1 - c_{crit})/Q$ (see Figure 9(a)). As noted above, $v = \sqrt{D/\beta}$ when $\tilde{p} = 4\beta(1 - c_{crit})/(3Q)$. For $\tilde{p} > p_{crit_2}$, $v < 0$ (i.e. the wave reverses direction, resulting in recovery of photoreceptors); however, since the wave stalls at $\tilde{p} = p_{crit_2}$ in practice, the wave would not reverse direction. Equation (47) also indicates that $v < 0$ when $\tilde{p} < p_{crit_1}$. In this case, the local photoreceptor density is sufficiently low that the local oxygen concentration exceeds the hyperoxic threshold, c_{crit}. As a result, degeneration would occur uniformly in such regions, and a travelling wave could not be established.

Figure 9(b) shows the variation in wave speed with eccentricity across the retina. We note that $v > 0$ for $\tilde{\theta}_{crit_4} < \theta < \tilde{\theta}_{crit_1}$ and $\theta > \tilde{\theta}_{crit_2}$, $v = 0$ for $\theta = \tilde{\theta}_{crit_1}$, $\theta = \tilde{\theta}_{crit_2}$ and $\theta = \tilde{\theta}_{crit_4}$, and $v < 0$ for $\theta < \tilde{\theta}_{crit_4}$ and $\tilde{\theta}_{crit_1} < \theta < \tilde{\theta}_{crit_2}$ (the latter two intervals are never penetrated by the travelling wave, since it will halt at their margins). The parameters $\tilde{\theta}_{crit_1}$, $\tilde{\theta}_{crit_2}$ and $\tilde{\theta}_{crit_4}$ correspond with (and are almost identical to) θ_{crit_1}, θ_{crit_2} and θ_{crit_4} from Section 3.2. Differences arise because we are dealing with the exact photoreceptor distribution, $\tilde{p}$, in the travelling wave analysis and the leading order photoreceptor distribution in the steady-state analysis.

In Figures 9(c) and (d) we compare our approximate expressions for the wave speed with those derived

from numerical simulations. Simulations equivalent to those in Section 3.3 were used to generate rightward and leftward travelling waves with either Michaelis-Menten ($Qpc/(\gamma + c)$) or constant (Qp) oxygen uptake. We consider the constant uptake case, in order to determine the effect of the non-linearity that characterises the Michaelis-Menten term on the wave speed, since this is not captured by our leading order approximation. The numerical wave speed at any given time point was calculated by measuring the distance moved by the wavefront (deemed to lie at $p(\theta, t) = 0.1$) over a fixed time step centred at the time point under consideration. We note that the numerical results are not smooth since they are estimated from a discrete spatial mesh. Since the travelling wave is initiated using a degenerate patch, the eccentricities over which leftward and rightward wave speeds can be calculated differ. The analytical and numerical results match well, though the analytical solution underestimates the wave speed near $\theta = 1$. This is more pronounced for rightward travelling waves, where the wave gives way to spatially uniform degeneration as the patch of preserved photoreceptors at the periphery narrows, bringing the whole of this region beneath the hyperoxic threshold. (The wave speed with constant oxygen uptake is smaller than that with Michaelis-Menten uptake since the rate of uptake is higher and, hence, the oxygen levels are lower in this case.) The numerical results also show that the direction of the wave influences its speed, travelling more quickly in the direction of decreasing photoreceptor density.

3.5. Mutation-induced Rod Degeneration

Having considered photoreceptor degeneration driven purely by hyperoxia, we now explore mutation-induced rod degeneration. We solve equations (11), (13)–(15) and (18), with $h(\theta, t) = 1$, using the method of lines as described in Section 3.3, where the equations for p_r and p_c are treated in the same way as the equation for p.

Figure 10 shows two typical patterns of degeneration that arise when mutation-induced rod loss is incorporated into the model. In Figure 10(a), the steady attrition of rods causes oxygen levels to rise across the retina. This leads to the development of hyperoxia at $\theta = 0.04$ and $\theta = 1$, where photoreceptor density is lowest, resulting in waves of hyperoxia-driven photoreceptor degeneration. These waves meet at $\theta = 0.32$ (corresponding to 25.3 degrees eccentricity), just to the right of the peak in photoreceptor density in the mid-periphery (at 23.7 degrees), whilst cone density is preserved at the centre of the fovea. The fact that degeneration spreads across the domain shows that the mutation-induced loss of rods has caused the mid-peripheral stable region to become unstable, whilst the preservation of cones at the centre of the retina demonstrates that the near-central stable region remains stable.

In Section 3.2 we predicted that mutation-induced rod degeneration could cause a stable patch to become unstable and spread. We test this prediction in Figure 10(b), where we remove a patch of photoreceptors between $\theta_1 = 0.70$ and $\theta_2 = 0.71$, which lies in the narrow portion of region A_2, extending to the right of region D_3 in Figure 3(a). As rods are lost, the patch becomes unstable, degenerating to the right (at $t = 6$) and to the left (at $t = 9$).

3.6. Mutation-induced Cone Degeneration

RP may also occur as a cone-rod dystrophy, involving a mutation-induced loss of cones. In this case, we solve equations (11), (13) and (18)–(20), with $h(\theta, t) = 1$, using the method of lines as described in Sections 3.3 and 3.5.

Figure 11 shows the results of a simulation with $F(\theta) = 1$. We note that hyperoxic degeneration initiates near the centre of the retina (at $t = 105$). If we decrease the hyperoxic threshold to $c_{crit} = 0.67$ (which is still high enough so as not to induce degeneration in a healthy retina), a second region of hyperoxic degeneration initiates, after the first, at $\theta = 1$, spreading inwards (results not shown). Only a minor increase in c_{crit} is required to prevent hyperoxic degeneration initiating at $\theta = 1$, since the initial density of cones at $\theta = 1$ is tiny, so that the effect of their loss on the oxygen profile in this region is subtle. We do not show a simulation

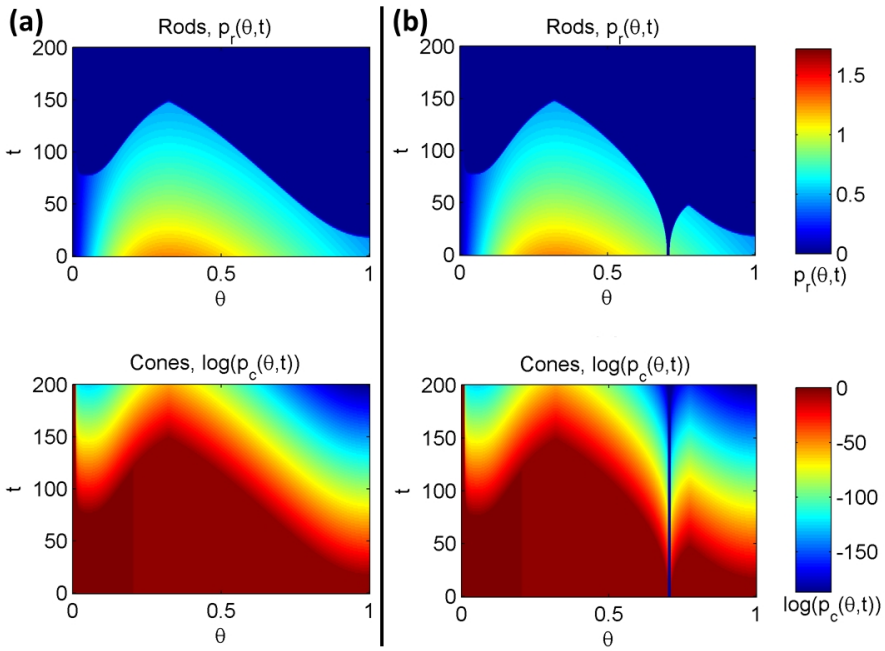

Figure 10: Dynamic simulations of photoreceptor loss and preservation with mutation-induced rod loss, with, (a), and without, (b), an initial degenerate patch. The colour bars apply to both graphs in the corresponding rows. Note that we plot the natural logarithm of the cone density, $\log(p_c)$. (a)–(b) Hyperoxic degeneration initiates at $\theta = 0.04$ and $\theta = 1$, spreading across the retina until all photoreceptors except those near $\theta = 0$ are lost. (b) Rod loss causes the degenerate patch to destabilise and expand. Equations (11), (13)–(15) and (18) were solved using the method of lines, with 4001 mesh points, $h(\theta, t) = 1$, (a) $F(\theta) = 1$ and (b) $F(\theta) = H(\theta - \theta_2) + H(\theta_1 - \theta)$. Parameter values: $\phi_r = 6.6 \times 10^{-3}$, (b) $\theta_1 = 0.70$ and $\theta_2 = 0.71$. Remaining parameter values as in Table 1.

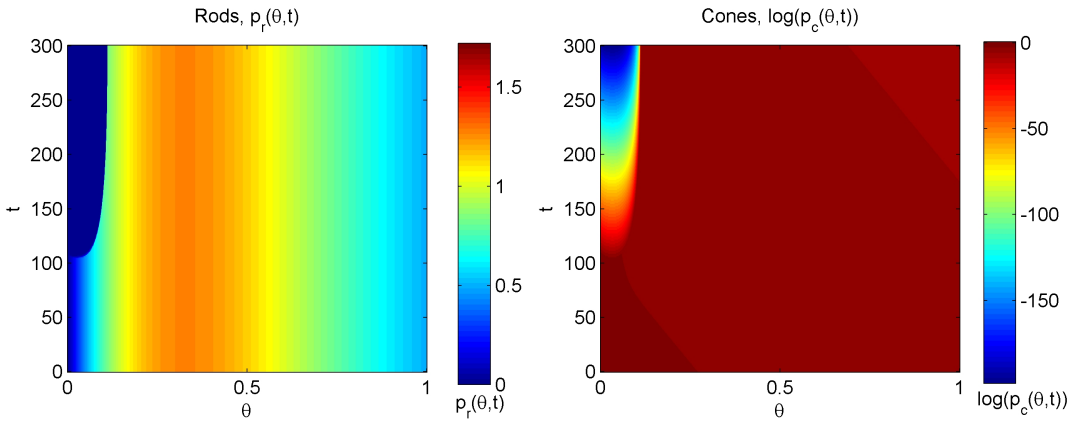

Figure 11: Dynamic simulation of photoreceptor loss and preservation with mutation-induced cone loss. Note that we plot the natural logarithm of the cone density, $\log(p_c)$. Hyperoxic degeneration initiates near the centre of the retina, eventually stalling as it propagates rightwards. Equations (11), (13) and (18)–(20) were solved using the method of lines, with 4001 mesh points, $h(\theta, t) = 1$ and $F(\theta) = 1$. Parameter values: $\phi_c = 6.6 \times 10^{-3}$. Remaining parameter values as in Table 1.

with an initial degenerate patch since, except near the centre of the retina, where degeneration occurs even in the absence of a patch, cone density is low, and so their loss is unlikely to destabilise a patch.

We have also considered the form of RP in which both rods and cones undergo the same rate of mutation-induced degeneration ($\phi_r = \phi_c = 6.6\times10^{-3}$, Hartong et al., 2006). The pattern of degeneration is very similar to that in Figure 10 for the case of mutation-induced rod loss, the key difference being that the central island of cones is eventually lost (results not shown).

3.7. Treatment

Antioxidants and trophic factors have shown promise in the treatment of RP. We model their effect via a sustained increase in the hyperoxic threshold c_{crit}, from $c_{crit} = c_{crit_1}$ to $c_{crit} = c_{crit_1} + c_{crit_2}$, at time $t = t_{crit}$ (see Section 2.4). In the absence of experimental data with which to estimate treatment parameters, we choose values to illustrate the qualitative behaviour of the system. In each case, we apply treatment after the initiation of hyperoxic degeneration, and, as before, we use the method of lines to solve the relevant equations.

In Figure 12 we examine the effect of treatment (applied at $t_{crit} = 20$) following the spread of an initial degenerate patch at $(\theta_1, \theta_2) = (0.03, 0.06)$. In this case, mutation-induced rod and cone degeneration are excluded, and equations (8), (9), (11) and (12) are solved, with $h(\theta, t) = 1$. In Figure 12(a), c_{crit} increases from 0.7 to 1 at $t = 20$. This corresponds to a strong treatment, since photoreceptors will remain healthy for oxygen concentrations close to the capillary concentration. In this case, degeneration halts and the degenerate patch shrinks to its original size. In Figure 12(b), c_{crit} increases from 0.7 to 0.8 at $t = 20$. For this mild treatment, degeneration halts as before, but regeneration is limited.

Figure 13(a) shows the effect of mild treatment ($c_{crit_2} = 0.1$) when mutation-induced rod degeneration is included. We solve equations (11), (13)–(15) and (18), with $h(\theta, t) = 1$, $t_{crit} = 25$ and an initial degenerate patch at $(\theta_1, \theta_2) = (0.70, 0.71)$. Without treatment, this problem is identical to that in Figure 10(b). We note that treatment delays the progression of hyperoxic degeneration.

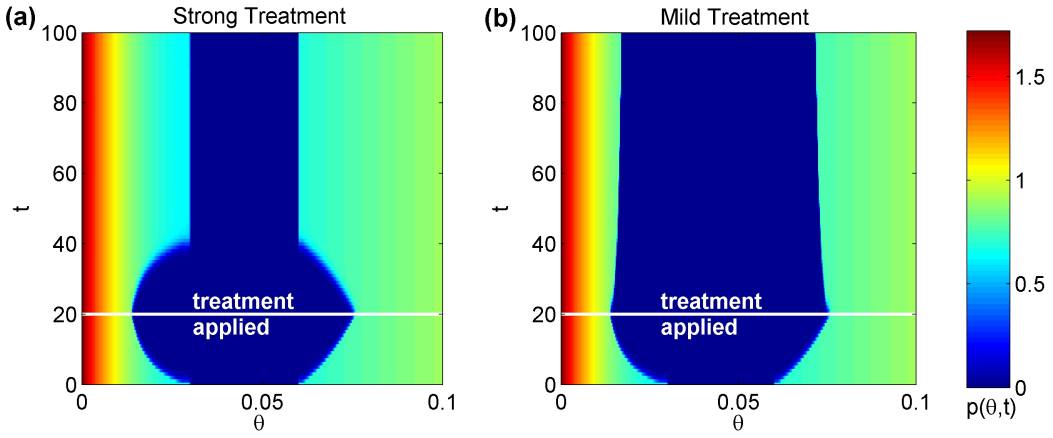

Figure 12: Dynamic simulations showing the effect of treatment upon photoreceptor loss and preservation. Strong treatment, (a), results in full recovery, whilst mild treatment, (b), results in minor recovery. Equations (8), (9), (11) and (12) were solved using the method of lines, with 4001 mesh points, $h(\theta, t) = 1$, $c_{crit}(t) = c_{crit_1} + c_{crit_2} H(t - t_{crit})$ and $F(\theta) = H(\theta - \theta_2) + H(\theta_1 - \theta)$. Parameter values: $\theta_1 = 0.03$, $\theta_2 = 0.06$, $c_{crit_1} = 0.7$, $t_{crit} = 20$, (a) $c_{crit_2} = 0.3$ and (b) $c_{crit_2} = 0.1$. Remaining parameter values as in Table 1.

Lastly, Figure 13(b) shows the effect of mild treatment ($c_{crit_2} = 0.1$) when mutation-induced cone degeneration is included. We solve equations (11), (13) and (18)–(20), with $h(\theta, t) = 1$, $t_{crit} = 150$ and without an initial degenerate patch. As such, without treatment, this problem is identical to that in Figure 11. We note that treatment halts the progression of hyperoxic degeneration, resulting in a minor recovery of rods.

4. Results: Model 2 — Capillary Degeneration

Thus far we have assumed that the capillary surface area per unit volume of tissue, $h(\theta, t)$, remains constant over time. In this section, we examine the effects of capillary loss upon the dynamics of photoreceptor degeneration.

4.1. Numerical Solution to the Steady-state Problem

We begin by examining the conditions under which a patch of photoreceptor loss will expand when it is also accompanied by a patch of capillary loss. For simplicity, we suppose the degenerate patch of photoreceptors extends from the ora serrata, at $\theta = 1$, to a point $\theta_p \in [0, 1)$. This is consistent with clinical observations which suggest that degeneration often initiates at the ora serrata (see, for example, Grover et al., 1998; Hamel, 2006; Hartong et al., 2006) and the results from Sections 3.5 and 3.6. Since capillary loss occurs in response to photoreceptor loss, we assume that it is confined to the region of the degenerate photoreceptor patch, such that its left-hand boundary $\theta_c \geq \theta_p$. We take the right-hand boundary of the degenerate capillary patch to lie at $\theta = 1$, since the degeneration of photoreceptors, and, hence, capillaries, is most likely to initiate here. As in Section 3.1, a degenerate patch will spread if the oxygen concentration on the edge of the patch is greater than or equal to the hyperoxic threshold, that is, if $c(\theta_p) \geq c_{crit}$.

As before, we construct numerical solutions to equations (8) and (11) using the finite difference method, with $p(\theta) = F(\theta)\tilde{p}(\theta)$ and $h(\theta) = G(\theta)$, where $F(\theta) = H(\theta_p - \theta)$ and $G(\theta) = H(\theta_c - \theta)$, for a range of values of θ_p and θ_c, where $\theta_p \leq \theta_c$.

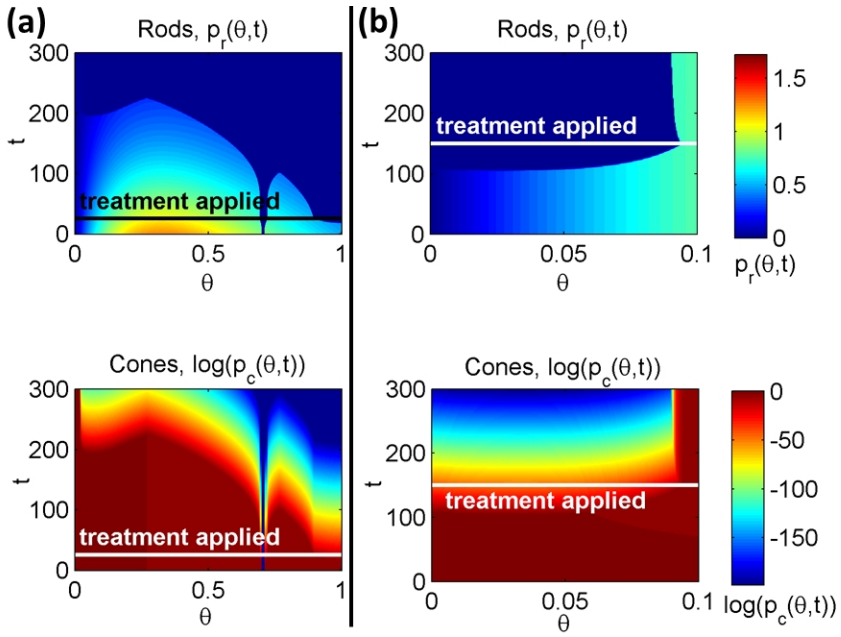

Figure 13: Dynamic simulations showing the effect of (mild) treatment upon photoreceptor loss and preservation with mutation-induced rod and cone loss. (a) Mutation-induced rod loss. (b) Mutation-induced cone loss. The colour bars apply to both graphs in the corresponding rows. Note that we plot the natural logarithm of the cone density, $\log(p_c)$. (a) Treatment delays hyperoxic degeneration. (b) Treatment results in a minor recovery of hyperoxic damage. Without treatment, simulations (a) and (b) would proceed as in Figures 10(b) and 11 respectively. (a) Equations (11), (13)–(15) and (18), and (b) equations (11), (13) and (18)–(20) were solved using the method of lines, with 4001 mesh points, $h(\theta,t) = 1$ and $c_{crit}(t) = c_{crit_1} + c_{crit_2} H(t - t_{crit})$. (a) $F(\theta) = H(\theta - \theta_2) + H(\theta_1 - \theta)$, (b) $F(\theta) = 1$. Parameter values: $c_{crit_1} = 0.7$, $c_{crit_2} = 0.1$, (a) $t_{crit} = 25$, $\theta_1 = 0.70$, $\theta_2 = 0.71$ and (b) $t_{crit} = 150$. Remaining parameter values as in Table 1.

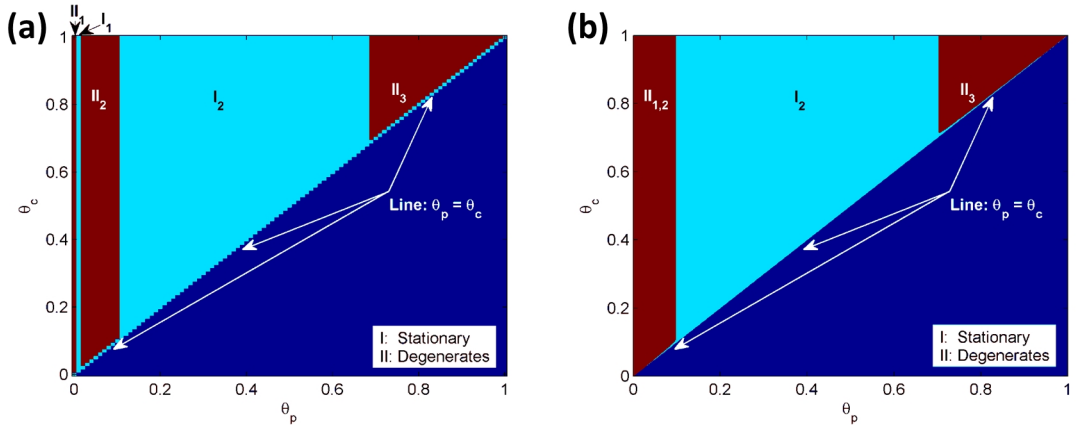

Figure 14: Diagrams to show stable and unstable regions in (θ_p, θ_c) parameter space as revealed by numerical simulations and asymptotic analysis. (a) Equations (8) and (11) were solved using the finite difference method, with 10,001 mesh points, and with $p(\theta) = H(\theta_p - \theta)\tilde{p}(\theta)$ and $h(\theta) = H(\theta_c - \theta)$, and (b) equation (48) was evaluated, for a range of values of both θ_p and θ_c, where $\theta_p \leq \theta_c$. If $c(\theta_p) < c_{crit}$, then the boundary at θ_p is stable; if $c(\theta_p) \geq c_{crit}$, then it is unstable. Parameter values as in Table 1.

Figure 14(a) shows the stability of the degenerate photoreceptor patch in (θ_p, θ_c) parameter space. We observe two stable (I_1 and I_2) and three unstable (II_1, II_2 and II_3) regions. The effect of capillary loss is seen only along the line $\theta_p = \theta_c$. Here capillary loss is coincident with photoreceptor loss, stabilising the patch. Comparison with Figure 3(a) reveals that region II_1 corresponds to regions D_1, B_1 and D_4, region I_1 to regions C_1, A_1 and C_3, region II_2 to regions D_2, B_2 and D_5, region I_2 to regions C_2 and A_2, and region II_3 to region D_3.

4.2. Mathematical Analysis of the Steady-state Problem

As in Section 3.2, we use asymptotic analysis to derive a leading order analytical expression for the oxygen concentration on the boundary of the degenerate patch of photoreceptors, and, thereby, determine its stability properties. (See the Supplementary Material for details of this analysis.) We consider the case where $p(\theta) = F(\theta)\tilde{p}(\theta)$ and $h(\theta) = G(\theta)$, where $F(\theta) = H(\theta_p - \theta)$ and $G(\theta) = H(\theta_c - \theta)$, for a range of values of θ_p and θ_c, where $0.1 < \theta_p \leq \theta_c < 1 - \omega\epsilon$, $\epsilon = O(10^{-2})$ and ω is a positive constant of $O(1)$, bounding θ_p and θ_c away from the margins of the domain in the same way as for θ_1 and θ_2 in Section 3.2 (see Figure S1 for a diagram showing the division of the domain into inner and outer regions).

Substituting $\theta = \theta_p$ into either of equations (S.6) or (S.7), we obtain the following expression for the concentration of oxygen on the edge of the degenerate patch of photoreceptors:

$$c_0(\theta_p) = 1 - \frac{Q}{2\beta}\left(1 + e^{-2\epsilon^{-1}\sqrt{\frac{\beta}{D}}(\theta_c - \theta_p)}\right)K(\theta_p), \tag{48}$$

where $K(\theta) := B_2 e^{-b_2\theta} + B_3\theta e^{-b_3\theta}$, as before. This expression is similar to equation (35), apart from a term that depends upon θ_c, which is exponentially small everywhere except where $\theta_c - \theta_p = O(\epsilon)$ (assuming $\theta_c \geq \theta_p$). Therefore, the degeneration of a patch of capillaries will not have a significant effect unless the inner margin of the capillary patch lies within a distance of $O(\epsilon)$ to the inner margin of the patch of photoreceptor loss.

This is demonstrated in Figure 14(b), which shows the regions in (θ_p, θ_c) parameter space where the degenerate patch of photoreceptors is stable or unstable. This figure was obtained by evaluating equation (48) for a range of values of $\theta_p \leq \theta_c$ and noting whether $c(\theta_p)$ exceeds the hyperoxic threshold, c_{crit}. In region I_2 the degenerate photoreceptor patch is stable, whereas in regions $\mathrm{II}_{1,2}$ and II_3 the degenerate photoreceptor patch is unstable, expanding centrally. (The correspondence between Figures 3(b) and 14(b) is due to the fact that θ_{crit_1} and θ_{crit_2} are preserved for $\theta_c - \theta_p > O(\epsilon)$.) Region I_2 also extends in a narrow region along the line $\theta_p = \theta_c$, beneath the unstable regions, becoming increasingly narrow as θ_p approaches 0 on the left, and 1 on the right. It is in this region, of width $O(\epsilon)$ or less, that capillary loss exerts an effect on the stability of the degenerate photoreceptor patch.

In the limiting case where $\theta_c = \theta_p$, equation (48) reduces to equation (25), with $\theta = \theta_p$. Since equation (25) gives the oxygen concentration under healthy conditions and since $c(\theta) < c_{crit}$ under healthy conditions, $c_0(\theta_p) < c_{crit}$ when $\theta_c = \theta_p$ and we deduce that the degenerate photoreceptor patch is always stable in this case. While our analysis does not hold for $\theta_p < 0.1$, numerical simulations show that the degenerate photoreceptor patch is also stable in this region when $\theta_c = \theta_p$ (see Figure 14(a)).

Setting $c_0(\theta_p) = c_{crit}$ in equation (48), we obtain the following expression for the critical position of the left-hand boundary of the degenerate capillary patch, $\theta_{c_{crit}}(\theta_p)$:

$$\theta_{c_{crit}}(\theta_p) = \theta_p + \frac{\epsilon}{2}\sqrt{\frac{D}{\beta}}\log\left(\frac{QK(\theta_p)}{2\beta(1-c_{crit}) - QK(\theta_p)}\right). \tag{49}$$

For a given value of θ_p, this expression allows us to calculate how far centrally the degenerate capillary patch must extend to prevent further photoreceptor loss, in those cases where photoreceptor loss would proceed in the absence of capillary loss. For $\theta_p = 1.8$ as in Figure S.1, $\theta_{c_{crit}}(\theta_p) = 1.802$ (3 d.p.), so that $\theta_{c_{crit}}(\theta_p) - \theta_p \leq O(\epsilon)$.

4.3. Numerical Solution to the Time-dependent Problem

Lastly, we consider the effect of capillary loss upon photoreceptor degeneration, following the loss of a patch of photoreceptors, or in response to mutation-induced rod or cone degeneration. In all cases we assume a healthy initial capillary distribution, $h_0(\theta) = 1$, and allow capillaries to degenerate subsequent to this in response to photoreceptor loss. We solve the time-dependent problems using the method of lines, in the same way as described in Section 3.3.

4.3.1. Degenerate Patch

Figure 15(a) shows how capillary degeneration affects the progression of a degenerate patch of photoreceptors. Since we do not know the *in vivo* rate of degeneration (to the best of our knowledge this has not been measured in RP, see Section 1), we take $\eta = 0$, 10^{-2}, 10^{-1}, 1 and 10, and find that it is sufficient to demonstrate the full range of behaviours (described below). We note that $\eta = 1$ corresponds to a dimensional value of $\eta = \delta = 10^{-7}$ s^{-1}, in which case the rate of capillary degeneration is equal to that of photoreceptors.

When $\eta = 10^{-2}$, degeneration is almost identical to that when $\eta = 0$. For $\eta = 10^{-1}$, significant degeneration is followed by complete recovery (not including the original degenerate patch). When $\eta = 1$, after an initial period of minimal photoreceptor loss, the system recovers fully (again, not including the original degenerate patch). Lastly, when $\eta = 10$, the patch remains stationary, with an almost imperceptible fluctuation in photoreceptor density early on. The model exhibits similar behaviours for other patch widths and locations (results not shown).

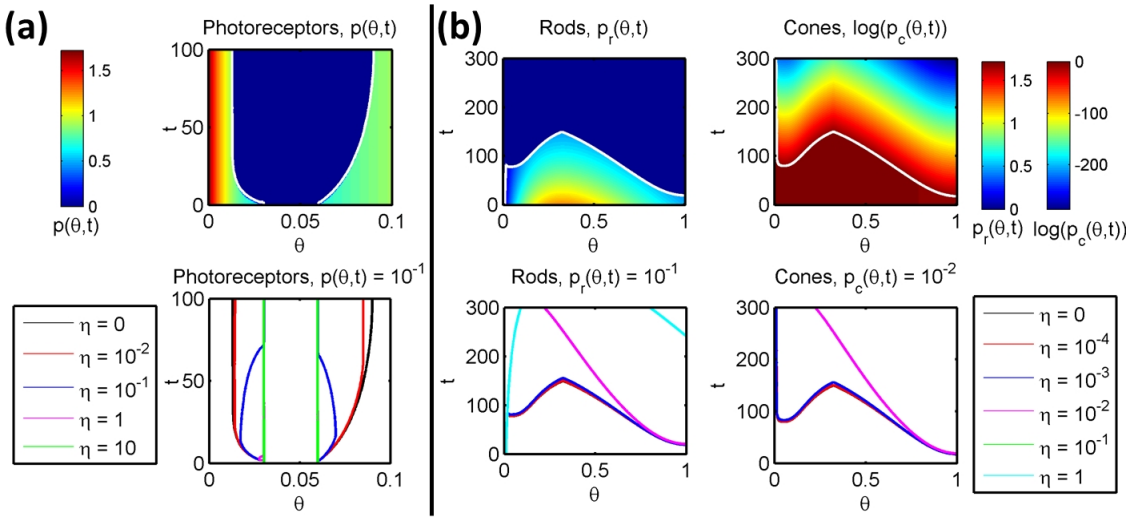

Figure 15: Series of plots comparing the progression of photoreceptor degeneration for a range of values of the capillary degeneration rate, η, following removal of a patch of photoreceptors from the interval $\theta \in [\theta_1, \theta_2]$ (a), or where the retina undergoes mutation-induced rod degeneration (b). Top row: $\eta = 0$ ((a) and (b)). Bottom row: $\eta = 0, 10^{-2}, \ldots, 10$ (a) and $\eta = 0, 10^{-4}, \ldots, 1$ (b). The white lines in the top row and the coloured lines in the bottom row mark the contours, $(\theta(t), t)$, along which $p(\theta, t) = 10^{-1}$ (photoreceptors and rods) or $p(\theta, t) = 10^{-2}$ (cones) and hence show the boundaries of the degenerate regions. In all cases, the spread of photoreceptor degeneration decreases with increasing η. Equations (8)–(12) (a), and (11), (13)–(16) and (18) (b) were solved using the method of lines, with 4001 mesh points, $F(\theta) = H(\theta - \theta_2) + H(\theta_1 - \theta)$ (a), $F(\theta) = 1$ (b) and $G(\theta) = 1$. Parameter values: $(\theta_1, \theta_2) = (0.03, 0.06)$ (a) and $\phi_r = 6.6 \times 10^{-3}$ (b). Remaining parameter values as in Table 1.

4.3.2. Mutation-induced Rod or Cone Degeneration

Figure 15(b) shows how capillary degeneration affects the loss of rods and cones, when the retina undergoes mutation-induced rod degeneration. This scenario is identical to that in Figure 10(a), where $\eta = 0$ (reproduced in the top row of Figure 15(b)). In this case, we take $\eta = 0$, 10^{-4}, 10^{-3}, 10^{-2}, 10^{-1} and 1, and observe the range of possible behaviours (described below).

When $\eta = 10^{-3}$ or 10^{-4}, degeneration proceeds as for $\eta = 0$. When $\eta = 10^{-2}$, the wave of hyperoxic degeneration proceeds more slowly. Lastly, when $\eta = 10^{-1}$ or 1, hyperoxic degeneration does not initiate, the contours appearing on the left and top-right of the bottom-left graph in Figure 15(b) being due to mutation-induced loss.

In the case of mutation-induced cone loss, the pattern of degeneration for $\eta = 10^{-3}$ and 10^{-4} is similar to that for $\eta = 0$, whilst hyperoxic degeneration does not initiate for $\eta = 10^{-2}$, 10^{-1} or 1 (results not shown).

5. Discussion

RP causes the progressive degeneration of photoreceptors. In humans, photoreceptor loss initiates in patches, which spread and coalesce until only a central island of photoreceptors remain, these also eventually being lost. RP typically exhibits as a rod-cone dystrophy, in which rod photoreceptors are affected earlier and more severely than cone photoreceptors; however, cone-rod dystrophies also occur, in which the reverse is true. It is not known what causes degenerate patches to spread, or why cone loss should follow rod loss in rod-cone dystrophies (and vice-versa in cone-rod dystrophies). The oxygen toxicity hypothesis posits hyperoxia as the mechanism underlying these phenomena.

We have derived a model to explore the dynamics of hyperoxia-driven photoreceptor degeneration in a human retina with RP. This is the first mathematical model to describe the oxygen toxicity hypothesis or to account for the distribution of photoreceptors. Our model reveals that degeneration may spread via hyperoxia and predicts specific spatio-temporal patterns of degeneration (described below).

Numerical and asymptotic analysis of the steady-state problem allow us to determine the stability properties of any given degenerate patch of photoreceptors (Sections 3.1 and 3.2). It was found that the retina can be divided into five regions, two stable and three unstable (see Figure 6). The margins of a wide (width $O(1)$) degenerate patch are stationary if they are located within stable regions. If a margin lies in an unstable region it travels outwards, expanding the patch size, until it reaches either the edge of the retina or the margin of a stable region. Surprisingly, the stability of a wide patch does not depend upon its width. This is because widely displaced margins are separated by an outer region, rendering their local oxygen concentrations independent from one another. Narrow patches (width $\leq O(\epsilon)$, where $\epsilon = O(10^{-2})$) remain stationary within stable regions and may persist within regions where wider patches would be unstable, provided they are sufficiently narrow (see Figure 3).

Numerical simulations of the time-dependent problem confirm the predictions from the steady-state analysis and also reveal that the wave speed of degeneration is negatively correlated with the local photoreceptor density (Section 3.3). Travelling wave analysis allows us to derive an analytical expression for the wave speed of degeneration, confirming that it is a monotone decreasing function of the local photoreceptor density (Section 3.4). Numerical simulations also show that the wave speed at a given eccentricity is greater when travelling in the direction of decreasing photoreceptor density than when travelling in the direction of increasing photoreceptor density. These results may be explained by the fact that the width of the region exposed to hyperoxia ahead of the wavefront is wider in regions with a lower local photoreceptor density. More detailed longitudinal studies are required to validate these model predictions.

In order to capture the rod-cone dystrophy form of RP, we incorporated mutation-induced, hyperoxia-independent rod degeneration into the model (Section 3.5). The progressive loss of rods causes oxygen

levels to rise across the retina, so that they exceed the hyperoxic threshold in some regions, initiating waves of hyperoxic degeneration. The model predicts that hyperoxia-driven photoreceptor loss will initiate at the ora serrata, spreading centrally, and later initiate in the para/perifoveal unstable region, spreading centrally and peripherally. The mutation-induced loss of rods causes the mid-peripheral stable region to shrink and eventually to vanish, allowing waves of hyperoxic degeneration to sweep across it, so that only a narrow island of cones at the centre of the fovea remains at the end stage. This matches well with the (pattern 1) peripheral to central progression observed in humans by Grover et al. (1998), and in particular with the form which includes a para/perifoveal ring scotoma (pattern 1B). Our model also predicts that mutation-induced rod loss may cause a stable degenerate patch of photoreceptors to become unstable and spread.

To explore the cone-rod dystrophy form of RP, we incorporated mutation-induced, hyperoxia-independent cone degeneration into the model (Section 3.6). The model predicts that hyperoxic degeneration will initiate near the centre of the retina, spreading toward the mid-peripheral stable region where degeneration stalls. It may also cause hyperoxic degeneration to initiate at the ora serrata at a later stage, spreading centrally to the mid-peripheral stable region. This pattern of progression is similar that observed in humans by Hamel (2007), though the complete preservation of the mid-peripheral stable region is not seen *in vivo*. We also considered the case involving the mutation-induced degeneration of both rods and cones. Our models predict that this will progress in a similar way to rod-cone dystrophy, the key difference being that central vision is not preserved.

Our analysis and simulations suggest that the retina is most susceptible to hyperoxic damage in two regions: the peripheral unstable region and the para/perifoveal unstable region (see Figure 6). Both regions correspond to local minima in the photoreceptor density where oxygen levels are highest. It is within these regions that degenerate patches are most likely to spread and it is here that hyperoxic degeneration initiates when mutation-induced rod or cone degeneration is included in the model. By contrast, regions with a high photoreceptor density act as a barrier to the spread of degeneration; the exception to this rule being the central unstable region, which is too narrow to support a healthy photoreceptor population when the surrounding retina is dystrophic. As a result, patterns of degeneration which involve a preferential loss of mid-peripheral photoreceptors, such as patterns 2 and 3 described by Grover et al. (1998), are unlikely to arise via hyperoxia-driven degeneration, though a 2D model, incorporating the azimuthal dimension, is needed to explore this possibility fully.

Simulations predict that, in the absence of mutation-induced cone loss, a narrow island of cones will remain intact at the centre of the fovea. This fits with the observation that central vision is generally the last to be lost in RP, but fails to replicate the eventual loss of cones observed in many patients. It may be that, whilst oxygen levels remain below the 'hyperoxic threshold', prolonged exposure to higher than normal oxygen levels proves toxic over time. Alternatively, or in addition to this, loss of structural support from neighbouring photoreceptors, the release of toxic substances by dying photoreceptors, the absence of rod trophic factor or the action of microglia could contribute to the demise of the cone island.

Our simulations suggest that treatment with antioxidants or trophic factors may prevent the initiation of hyperoxic degeneration, that it may delay or halt degeneration, or allow some recovery of damaged photoreceptors (Section 3.7). Mathematically this occurs by increasing the hyperoxic threshold and hence the widths of the stable regions. Recovery is likely to be partial at best since many photoreceptors will have died or degenerated beyond recovery prior to treatment; therefore, the total recovery seen in Figure 12(a) is overly optimistic. Nonetheless, both antioxidants and trophic factors have been found to be effective in slowing photoreceptor degeneration (Dong et al., 2006; Komeima et al., 2006, 2007; Okoye et al., 2003; Sanz et al., 2007; Yamada et al., 2001; Yu et al., 2004) and it has been shown that both rod and cone photoreceptors may regain OS length and function following light damage (Chrysostomou et al., 2008; Lee et al., 2012). Hence, partial recovery may be realistic. Treatment would need to be maintained throughout the lifetime

of the patient, otherwise degeneration would resume. Antioxidants and trophic factors could be supplied over the long-term using either encapsulated cell technology or ocular gene therapy (see, for example, Dong et al., 2006; Musarella and MacDonald, 2011; Orosz et al., 2004; Tao, 2006; Tao et al., 2002; Wen et al., 2012). If treatment could be targeted to specific regions of the retina, our results suggest that the unstable peripheral and para/perifoveal regions should be targeted, as they are most susceptible to hyperoxic damage.

Numerical and asymptotic analysis of the capillary loss problem shows that capillary loss must extend to within $O(\epsilon)$ of, and be essentially coincident with, the margins of a degenerate photoreceptor patch to prevent further photoreceptor degeneration in those cases where it would proceed in the absence of capillary loss (Sections 4.1 and 4.2). This somewhat counter-intuitive result derives from the fact that the presence of the degenerate patch of capillaries can only influence the oxygen concentration at the edge of the patch of photoreceptor loss if it lies within the ($O(\epsilon)$ in width) boundary layer extending from the edge of the degenerate photoreceptor patch. This model prediction could be tested experimentally, using a laser to ablate the choroid in those regions from which photoreceptors are absent. This could also be used as a treatment strategy for RP, similar to those presently used to treat macular degeneration (see, for instance, Coleman et al., 2008; Jager et al., 2008).

Numerical simulations of the time-dependent capillary loss problem reveal that capillary degeneration may prevent, halt, delay or reverse photoreceptor degeneration, though recovery is likely to be limited *in vivo* (Section 4.3). Further experimental work is needed to determine the rate of capillary degeneration and thereby to predict its effect upon photoreceptor degeneration.

Future work could include a more detailed description of the biochemistry underlying hyperoxic damage, and the action of antioxidants and trophic factors. This would require, or could proceed in tandem with, experimental work, to elucidate the relevant pathways. Instead of the direct dependence of the CC upon photoreceptors assumed in this paper, the complex interdependence of photoreceptors, RPE, CC and VEGF could be captured in the model (assuming the cellular and biochemical details could be experimentally determined). The model could also be extended to 2D by including the azimuthal dimension, allowing us to more fully explore the patterns of photoreceptor loss to which the oxygen toxicity mechanism could give rise. Lastly, a similar approach to that used here, accounting for the regional variation in rod and cone density, could also be used to investigate the rod trophic factor and rod toxic substance hypotheses.

In conclusion, the oxygen toxicity hypothesis can account for some of the patterns of photoreceptor degeneration found in RP, which can be explained in terms of the arrangement of stable and unstable regions within the retina. The wave speed of hyperoxic degeneration is a monotone decreasing function of the local photoreceptor density. Both treatment with antioxidants and trophic factors, as well as capillary loss, are predicted to prevent, halt, delay or reverse photoreceptor degeneration, whilst a patch of capillary loss would need to be essentially coincident with the edge of a patch of photoreceptor loss in order to prevent further photoreceptor degeneration.

Acknowledgements

We gratefully acknowledge the Engineering and Physical Sciences Research Council (EPSRC) in the UK for funding through a studentship at the Systems Biology programme of the University of Oxford's Doctoral Training Centre P.A.R. We also thank the anonymous reviewers for their helpful and insightful comments.

References

Bender, C. M., Orszag, S. A., 1999. Advanced Mathematical Methods for Scientists and Engineers I: Asymptotic Methods and Perturbation Theory. Springer.

Burns, J., Clarke, G., Lumsden, C. J., 2002. Photoreceptor death: Spatiotemporal patterns arising from one-hit death kinetics and a diffusible cell death factor. Bull. Math. Biol. 64, 1117–1145.

Camacho, E. T., Colón Vélez, M. A., Hernández, D. J., Bernier, U. R., van Laarhoven, J., Wirkus, S., 2010. A mathematical model for photoreceptor interactions. J. Theor. Biol. 267 (4), 638–646.

Camacho, E. T., Léveillard, T., Sahel, J. A., Wirkus, S., 2016a. Mathematical model of the role of RdCVF in the coexistence of rods and cones in a healthy eye. Bull. Math. Biol. 78 (7), 1394–1409.

Camacho, E. T., Melara, L. A., Villalobos, M. C., Wirkus, S., 2014. Optimal control in the treatment of retinitis pigmentosa. Bull. Math. Biol. 76 (2), 292–313.

Camacho, E. T., Punzo, C., Wirkus, S. A., 2016b. Quantifying the metabolic contribution to photoreceptor death in retinitis pigmentosa via a mathematical model. J. Theor. Biol. 408, 75–87.

Camacho, E. T., Radulescu, A., Wirkus, S., 2016c. Bifurcation analysis of a photoreceptor interaction model for retinitis pigmentosa. Commun. Nonlinear Sci. Numer. Simulat. 38, 267–276.

Camacho, E. T., Wirkus, S., 2013. Tracing the progression of retinitis pigmentosa via photoreceptor interactions. J. Theor. Biol. 317 (0), 105–118.

Chrysostomou, V., Stone, J., Stowe, S., Barnett, N. L., Valter, K., 2008. The status of cones in the rhodopsin mutant P23H-3 retina: Light-regulated damage and repair in parallel with rods. Invest. Ophthalmol. Vis. Sci. 49 (3), 1116–1125.

Cideciyan, A. V., Hood, D. C., Huang, Y., Banin, E., Li, Z.-Y., Stone, E. M., Milam, A. H., Jacobson, S. G., 1998. Disease sequence from mutant rhodopsin allele to rod and cone photoreceptor degeneration in man. Proc. Natl. Acad. Sci. 95 (12), 7103–7108.

Cingolani, C., Rogers, B., Lu, L., Kachi, S., Shen, J., Campochiaro, P. A., 2006. Retinal degeneration from oxidative damage. Free Radic. Biol. Med. 40 (4), 660–669.

Clarke, G., Collins, R. A., Leavitt, B. R., Andrews, D. F., Hayden, M. R., Lumsden, C. J., McInnes, R. R., 2000. A one-hit model of cell death in inherited neuronal degenerations. Nature 406, 195–199.

Clarke, G., Lumsden, C. J., 2005a. Heterogeneous cellular environments modulate one-hit neuronal death kinetics. Brain Res. Bull. 65 (1), 59–67.

Clarke, G., Lumsden, C. J., 2005b. Scale-free neurodegeneration: cellular heterogeneity and the stretched exponential kinetics of cell death. J. Theor. Biol. 233 (4), 515–525.

Clarke, G., Lumsden, C. J., McInnes, R. R., 2001. Inherited neurodegenerative diseases: the one-hit model of neurodegeneration. Hum. Mol. Genet. 10 (20), 2269–2275.

Coleman, H. R., Chan, C. C., Ferris III, F. L., Chew, E. Y., 2008. Age-related macular degeneration. Lancet 372 (9652), 1835–1845.

Colón Vélez, M. A., Hernández, D. J., Bernier, U. R., van Laarhoven, J., Camacho, E. T., 2003. Mathematical models for photoreceptor interactions. Tech. rep., Cornell University, Department of Biological Statistics and Computational Biology.

Curcio, C. A., Millican, C. L., Allen, K. A., Kalina, R. E., 1993. Aging of the human photoreceptor mosaic: evidence for selective vulnerability of rods in central retina. Invest. Ophthalmol. Vis. Sci. 34 (12), 3278–3296.

Curcio, C. A., Sloan, K. R., Kalina, R. E., Hendrickson, A. E., 1990. Human photoreceptor topography. J. Comp. Neurol. 292 (4), 497–523.

Del Priore, L. V., Kaplan, H. J., Hornbeck, R., Jones, Z., Swinn, M., 1996. Retinal pigment epithelial debridement as a model for the pathogenesis and treatment of macular degeneration. Am. J. Ophthalmol. 122 (5), 629–643.

Dong, A., Shen, J., Krause, M., Akiyama, H., Hackett, S. F., Lai, H., Campochiaro, P. A., 2006. Superoxide dismutase 1 protects retinal cells from oxidative damage. J. Cell Physiol. 208 (3), 516–526.

Escher, P., Tran, H. V., Vaclavik, V., Borruat, F. X., Schorderet, D. F., Munier, F. L., 2012. Double concentric autofluorescence ring in NR2E3-p.G56R-linked autosomal dominant retinitis pigmentosa. Invest. Ophthalmol. Vis. Sci. 53 (8), 4754–4764.

Fintz, A. C., Audo, I., Hicks, D., Mohand-Saïd, S., Léveillard, T., Sahel, J., 2003. Partial characterization of retina-derived cone neuroprotection in two culture models of photoreceptor degeneration. Invest. Ophthalmol. Vis. Sci. 44 (2), 818–825.

García-Ayuso, D., Ortín-Martínez, A., Jiménez-López, M., Galindo-Romero, C., Cuenca, N., Pinilla, I., Vidal-Sanz, M., Agudo-Barriuso, M., Villegas-Pérez, M. P., 2013. Changes in the photoreceptor mosaic of P23H-1 rats during retinal degeneration: Implications for rod-cone dependent survival. Invest. Ophthalmol. Vis. Sci. 54 (8), 5888–5900.

Grover, S., Fishman, G. A., Brown Jr, J., 1998. Patterns of visual field progression in patients with retinitis pigmentosa. Ophthalmology 105 (6), 1069–1075.

Gupta, N., Brown, K. E., Milam, A. H., 2003. Activated microglia in human retinitis pigmentosa, late-onset retinal degeneration, and age-related macular degeneration. Exp. Eye Res. 76 (4), 463–471.

Hamel, C., 2006. Retinitis pigmentosa. Orphanet. J. Rare Dis. 1 (1), 40.

Hamel, C., 2007. Cone rod dystrophies. Orphanet. J. Rare Dis. 2 (1), 7.

Hartong, D. T., Berson, E. L., Dryja, T. P., 2006. Retinitis pigmentosa. Lancet 368 (9549), 1795–1809.

Jager, R. D., Mieler, W. F., Miller, J. W., 2008. Age-related macular degeneration. N. Engl. J. Med. 358 (24), 2606–2617.

Ji, Y., Zhu, C. L., Grzywacz, N. M., Lee, E. J., 2012. Rearrangement of the cone mosaic in the retina of the rat model of retinitis pigmentosa. J. Comp. Neurol. 520 (4), 874–888.

Kohen, R., Nyska, A., 2002. Invited review: Oxidation of biological systems: Oxidative stress phenomena, antioxidants, redox reactions, and methods for their quantification. Toxicol. Pathol. 30 (6), 620–650.

Komeima, K., Rogers, B., Lu, L., Campochiaro, P., 2006. Antioxidants reduce cone cell death in a model of retinitis pigmentosa. Proc. Natl. Acad. Sci. 103 (30), 11300–11305.

Komeima, K., Rogers, B. S., Campochiaro, P. A., 2007. Antioxidants slow photoreceptor cell death in mouse models of retinitis pigmentosa. J. Cell Physiol. 213 (3), 809–815.

Lee, D. C., Vazquez-Chona, F. R., Ferrell, W. D., Tam, B. M., Jones, B. W., Marc, R. E., Moritz, O. L., 2012. Dysmorphic photoreceptors in a P23H mutant rhodopsin model of retinitis pigmentosa are metabolically active and capable of regenerating to reverse retinal degeneration. J. Neurosci. 32 (6), 2121–2128.

Lee, E. J., Ji, Y., Zhu, C. L., Grzywacz, N. M., 2011. Role of Müller cells in cone mosaic rearrangement in a rat model of retinitis pigmentosa. Glia 59 (7), 1107–1117.

Léveillard, T., Mohand-Saïd, S., Lorentz, O., Hicks, D., Fintz, A. C., Clérin, E., Simonutti, M., Forster, V., Cavusoglu, N., Chalmel, F., Dollé, P., Poch, O., Lambrou, G., Sahel, J. A., 2004. Identification and characterization of rod-derived cone viability factor. Nat. Genet. 36 (7), 755–759.

Li, Z. Y., Possin, D. E., Milam, A. H., 1995. Histopathology of bone spicule pigmentation in retinitis pigmentosa. Ophthalmology 102 (5), 805–816.

Lima, L. H., Burke, T., Greenstein, V. C., Chou, C. L., Cella, W., Yannuzzi, L. A., Tsang, S. H., 2012. Progressive constriction of the hyperautofluorescent ring in retinitis pigmentosa. Am. J. Ophthalmol. 153 (4), 718–727.

Lima, L. H., Cella, W., Greenstein, V. C., Wang, N. K., Busuioc, M., Smith, R. T., Yannuzzi, L. A., Tsang, S. H., 2009. Structural assessment of hyperautofluorescent ring in patients with retinitis pigmentosa. Retina 29 (7), 1025–1031.

Lomasko, T., Clarke, G., Lumsden, C. J., 2007a. One-hit stochastic decline in a mechanochemical model of cytoskeleton-induced neuron death I: Cell-fate arrival times. J. Theor. Biol. 249 (1), 1–17.

Lomasko, T., Clarke, G., Lumsden, C. J., 2007b. One-hit stochastic decline in a mechanochemical model of cytoskeleton-induced neuron death II: Transition state metastability. J. Theor. Biol. 249 (1), 18–28.

Lomasko, T., Lumsden, C. J., 2009. One-hit stochastic decline in a mechanochemical model of cytoskeleton-induced neuron death III: Diffusion pulse death zones. J. Theor. Biol. 256 (1), 104–116.

Milam, A. H., Zong, Y. L., Fariss, R. N., 1998. Histopathology of the human retina in retinitis pigmentosa. Prog. Retin. Eye Res. 17 (2), 175–205.

Mohand-Saïd, S., Deudon-Combe, A., Hicks, D., Simonutti, M., Forster, V., Fintz, A. C., Léveillard, T., Dreyfus, H., Sahel, J. A., 1998. Normal retina releases a diffusible factor stimulating cone survival in the retinal degeneration mouse. Proc. Natl. Acad. Sci. 95 (14), 8357–8362.

Mohand-Saïd, S., Hicks, D., Dreyfus, H., Sahel, J. A., 2000. Selective transplantation of rods delays cone loss in a retinitis pigmentosa model. Arch. Ophthalmol. 118 (6), 807–811.

Mohand-Saïd, S., Hicks, D., Simonutti, M., Tran-Minh, D., Deudon-Combe, A., Dreyfus, H., Silverman, M. S., Ogilvie, J. M., Tenkova, T., Sahel, J., 1997. Photoreceptor transplants increase host cone survival in the retinal degeneration (rd) mouse. Ophthalmic Res. 29, 290–297.

Mullins, R. F., Kuehn, M. H., Radu, R. A., Enriquez, G. S., East, J. S., Schindler, E. I., Travis, G. H., Stone, E. M., 2012. Autosomal recessive retinitis pigmentosa due to ABCA4 mutations: Clinical, pathologic, and molecular characterization. Invest. Ophthalmol. Vis. Sci. 53 (4), 1883–1894.

Murakami, T., Akimoto, M., Ooto, S., Suzuki, T., Ikeda, H., Kawagoe, N., Takahashi, M., Yoshimura, N., 2008. Association between abnormal autofluorescence and photoreceptor disorganization in retinitis pigmentosa. Am. J. Ophthalmol. 145 (4), 687–694.

Musarella, M. A., MacDonald, I. M., 2011. Current concepts in the treatment of retinitis pigmentosa. J. Ophthalmol. 2011, 753547.

Okoye, G., Zimmer, J., Sung, J., Gehlbach, P., Deering, T., Nambu, H., Hackett, S., Melia, M., Esumi, N., Zack, D. J., Campochiaro, P. A., 2003. Increased expression of brain-derived neurotrophic factor preserves retinal function and slows cell death from rhodopsin mutation or oxidative damage. J. Neurosci. 23 (10), 4164–4172.

Orosz, K. E., Gupta, S., Hassink, M., Abdel-Rahman, M., Moldovan, L., Davidorf, F. H., Moldovan, N. I., 2004. Delivery of antiangiogenic and antioxidant drugs of ophthalmic interest through a nanoporous inorganic filter. Mol. Vis. 10, 555–565.

Oyster, C. W., 1999. The Human Eye: Structure and Function. Sinauer Associates Inc.

Padnick-Silver, L., Derwent, J. J. K., Giuliano, E., Narfström, K., Linsenmeier, R. A., 2006. Retinal oxygenation and oxygen metabolism in abyssinian cats with a hereditary retinal degeneration. Invest. Ophthalmol. Vis. Sci. 47 (8), 3683–3689.

Popović, P., Jarc-Vidmar, M., Hawlina, M., 2005. Abnormal fundus autofluorescence in relation to retinal function in patients with retinitis pigmentosa. Graefes Arch. Clin. Exp. Ophthalmol. 243, 1018–1027.

Ripps, H., 2002. Cell death in retinitis pigmentosa: Gap junctions and the 'bystander' effect. Exp. Eye Res. 74 (3), 327–336.

Roberts, P. A., 2015. Mathematical models of the retina in health and disease. D.Phil. thesis, University of Oxford.

Roberts, P. A., Gaffney, E. A., Luthert, P. J., Foss, A. J. E., Byrne, H. M., 2016. Mathematical and computational models of the retina in health, development and disease. Prog. Retin. Eye. Res. 53, 48–69.

Robson, A. G., Egan, C. A., Luong, V. A., Bird, A. C., Holder, G. E., Fitzke, F. W., 2004. Comparison of fundus autofluorescence with photopic and scotopic fine-matrix mapping in patients with retinitis pigmentosa and normal visual acuity. Invest. Ophthalmol. Vis. Sci. 45 (11), 4119–4125.

Robson, A. G., El-Amir, A., Bailey, C., Egan, C. A., Fitzke, F. W., Webster, A. R., Bird, A. C., Holder, G. E., 2003. Pattern ERG correlates of abnormal fundus autofluorescence in patients with retinitis pigmentosa and normal visual acuity. Invest. Ophthalmol. Vis. Sci. 44 (8), 3544–3550.

Robson, A. G., Michaelides, M., Saihan, Z., Bird, A. C., Webster, A. R., Moore, A. T., Fitzke, F. W., Holder, G. E., 2008. Functional characteristics of patients with retinal dystrophy that manifest abnormal parafoveal annuli of high density fundus autofluorescence; a review and update. Doc. Ophthalmol. 116 (2), 79–89.

Robson, A. G., Saihan, Z., Jenkins, S. A., Fitzke, F. W., Bird, A. C., Webster, A. R., Holder, G. E., 2006. Functional characterisation and serial imaging of abnormal fundus autofluorescence in patients with retinitis pigmentosa and normal visual acuity. Br. J. Ophthalmol. 90 (4), 472–479.

Robson, A. G., Tufail, A., Fitzke, F., Bird, A. C., Moore, A. T., Holder, G. E., Webster, A. R., 2011. Serial imaging and structure-function correlates of high-density rings of fundus autofluorescence in retinitis pigmentosa. Retina 10(10), 1–10.

Sahaboglu, A., Paquet-Durand, O., Dietter, J., Dengler, K., Bernhard-Kurz, S., Ekstrom, P. A. R., Hitzmann, B., Ueffing, M., Paquet-Durand, F., 2013. Retinitis pigmentosa: rapid neurodegeneration is governed by slow cell death mechanisms. Cell Death. Dis. 4, e488.

Sanz, M. M., Johnson, L. E., Ahuja, S., Ekström, P. A. R., Romero, J., van Veen, T., 2007. Significant photoreceptor rescue by treatment with a combination of antioxidants in an animal model for retinal degeneration. Neuroscience 145 (3), 1120–1129.

Shen, J., Yang, X., Dong, A., Petters, R. M., Peng, Y. W., Wong, F., Campochiaro, P. A., 2005. Oxidative damage is a potential cause of cone cell death in retinitis pigmentosa. J. Cell Physiol. 203 (3), 457–464.

Shintani, K., Shechtman, D. L., Gurwood, A. S., 2009. Review and update: Current treatment trends for patients with retinitis pigmentosa. Optometry 80 (7), 384–401.

Stone, J., Maslim, J., Valter-Kocsi, K., Mervin, K., Bowers, F., Chu, Y., Barnett, N., Provis, J., Lewis, G., Fisher, S. K., Bistid, S., Gargini, C., Cervetto, L., Merin, S., Pe'er, J., 1999. Mechanisms of photoreceptor death and survival in mammalian retina. Prog. Retin. Eye Res. 18(6), 689–735.

Tao, W., 2006. Application of encapsulated cell technology for retinal degenerative diseases. Expert Opin. Biol. Ther. 6 (7), 717–726.

Tao, W., Wen, R., Goddard, M. B., Sherman, S. D., O'Rourke, P. J., Stabila, P. F., Bell, W. J., Dean, B. J., Kauper, K. A., Budz, V. A., Tsiaras, W. G., Acland, G. M., Pearce-Kelling, S., Laties, A. M., Aguirre, G. D., 2002. Encapsulated cell-based delivery of CNTF reduces photoreceptor degeneration in animal models of retinitis pigmentosa. Invest. Ophthalmol. Vis. Sci. 43 (10), 3292–3298.

Travis, G. H., Sutcliffe, J. G., Bok, D., 1991. The retinal degeneration slow (rds) gene product is a photoreceptor disc membrane-associated glycoprotein. Neuron 6 (1), 61–70.

Valter, K., Maslim, J., Bowers, F., Stone, J., 1998. Photoreceptor dystrophy in the RCS rat: roles of oxygen, debris, and bFGF. Invest. Ophthalmol. Vis. Sci. 39 (12), 2427–2442.

Wang, X., Ryter, S. W., Dai, C., Tang, Z. L., Watkins, S. C., Yin, X. M., Song, R., Choi, A. M. K., 2003. Necrotic cell death in response to oxidant stress involves the activation of the apoptogenic Caspase-8/Bid pathway. J. Biol. Chem. 278 (31), 29184–29191.

Wangsa-Wirawan, N. D., Linsenmeier, R. A., 2003. Retinal oxygen: Fundamental and clinical aspects. Arch. Ophthalmol. 121 (4), 547–557.

Wellard, J., Lee, D., Valter, K., Stone, J., 2005. Photoreceptors in the rat retina are specifically vulnerable to both hypoxia and hyperoxia. Vis. Neurosci. 22 (4), 501–507.

Wen, R., Tao, W., Li, Y., Sieving, P. A., 2012. CNTF and retina. Prog. Retin. Eye Res. 31 (2), 136–151.

Yamada, H., Yamada, E., Ando, A., Esumi, N., Bora, N., Saikia, J., Sung, C.-H., Zack, D. J., Campochiaro, P. A., 2001. Fibroblast growth factor-2 decreases hyperoxia-induced photoreceptor cell death in mice. Am. J. Pathol. 159 (3), 1113–1120.

Yamada, H., Yamada, E., Hackett, S. F., Ozaki, H., Okamoto, N., Campochiaro, P. A., 1999. Hyperoxia causes decreased expression of vascular endothelial growth factor and endothelial cell apoptosis in adult retina. J. Cell Physiol. 179 (2), 149–156.

Young, R. W., 1967. The renewal of photoreceptor cell outer segments. J. Cell Biol. 33 (1), 61–72.

Young, R. W., 1971. The renewal of rod and cone outer segments in the rhesus monkey. J. Cell Biol. 49, 303–318.

Young, R. W., 1978. The daily rhythm of shedding and degradation of rod and cone outer segment membranes in the chick retina. Invest. Ophthalmol. Vis. Sci. 17 (2), 105–16.

Young, R. W., Bok, D., 1969. Participation of the retinal pigment epithelium in the rod outer segment renewal process. J. Cell Biol. 42, 392–403.

Yu, D. Y., Cringle, S., Valter, K., Walsh, N., Lee, D., Stone, J., 2004. Photoreceptor death, trophic factor expression, retinal oxygen status, and photoreceptor function in the P23H rat. Invest. Ophthalmol. Vis. Sci. 45 (6), 2013–2019.

Yu, D. Y., Cringle, S. J., 2001. Oxygen distribution and consumption within the retina in vascularised and avascular retinas and in animal models of retinal disease. Prog. Retin. Eye Res. 20 (2), 175–208.

Yu, D. Y., Cringle, S. J., 2005. Retinal degeneration and local oxygen metabolism. Exp. Eye Res. 80 (6), 745–751.

Yu, D. Y., Cringle, S. J., Su, E. N., Yu, P. K., 2000. Intraretinal oxygen levels before and after photoreceptor loss in the RCS rat. Invest. Ophthalmol. Vis. Sci. 41 (12), 3999–4006.

Zhu, C. L., Ji, Y., Lee, E.-J., Grzywacz, N. M., 2013. Spatiotemporal pattern of rod degeneration in the S334ter-line-3 rat model of retinitis pigmentosa. Cell Tissue Res. 351 (1), 29–40.